AD-A273 840

||||||||||||||||||||

DTIC
S ELECTE
DEC 16 1993
A

CHARACTERIZATION OF NONLINEAR EFFECTS IN
OPTICALLY PUMPED
VERTICAL CAVITY SURFACE EMITTING LASERS

THESIS

Scott L. Brown, Captain, USAF

AFIT/GEO/ENP/93D-01

93-30508
||||||||||||||||||||

Approved for public release; distribution unlimited

93 12 1 51 32

Best
Available
Copy

CHARACTERIZATION OF NONLINEAR EFFECTS IN
OPTICALLY PUMPED
VERTICAL CAVITY SURFACE EMITTING LASERS

THESIS

Presented to the Faculty of the Graduate School of Engineering

of the Air Force Institute of Technology

Air University

In Partial Fulfillment of the

Requirements for the Degree of

Master of Science in Electrical Engineering

Scott L. Brown, B.S.

Captain, USAF

AFIT/GEO/ENP/93D-01

December 1993

Accesion For		
NTIS CRA&I		⋃
DTIC TAB		
Unannounced		
Justification		
By		
Distribution /		
Availability Codes		
Dist	Avail and/or Special	
A-1		

Approved for public release; distribution unlimited

Preface

Vertical Cavity Surface Emitting Lasers (VCSELs) are an exciting new technology of semiconductor lasers which have potential applications in fiber optic communications, optical computing, and two dimensional arrays due to their very small size and spectral purity. The research I performed for this thesis is notable for not only the results (in which we observed a couple of things not reported before), but also the optical setup which was unique in that it allowed me to make several different observations simultaneously. Although I began to question the advantages of optically pumping the VCSEL over electrical pumping, I believe my setup maximized those advantages.

I enjoyed my research and learned much more than I could put in this document. I would to thank my good luck for having arrived just as $200K of new laser equipment became operational. To Captain Jeff Grantham, thanks for your patience, understanding, and availability--I am so glad I went with this project! To Greg Vansuch, thanks for listening, being patient, and explaining things ad infinitum-- if I where smarter we'd make a great team. Likewise to Rich Bagnell; thanks for finding the time to help us. To Rick Patton, your assistance was appreciated. And finally, for technical, emotional, and diversionary assistance as well as many other intangibles, I wish to thank Mari--thank-you.

And now it's off to Headquarters AFSPACECOM to put my electro-optic degree to practice... Well, at least it's in Colorado.

<div align="right">Scott Brown</div>

Table of Contents

List of Figures

List of Tables

AFIT/GEO/ENP/93D-01

Abstract

The nonlinear characteristics of optically pumped Vertical Cavity Surface Emitting Lasers (VCSELs) are identified, isolated, and quantified. Three different VCSELs are evaluated including two with gain regions of bulk GaAs operating at 875nm and one multi-quantum well (MQW) InGaAs VCSEL operating at 950nm. The nonlinearities evaluated include those due to cavity temperature, carrier injection, and internal lasing field. The VCSELs are pumped by a picosecond/femtosecond Ti:Sapphire laser which is configured to operate in CW, gated CW (minimum gate width was 200ns), picosecond, and gated picosecond modes. A linear relationship is shown between wavelength and substrate temperature, cavity temperature, and injected carriers. The redshift in output wavelength for increases in internal temperature is quantified. It is shown that heating is the dominate nonlinearity in the bulk gain region VCSELs for the pump duty cycles which could be achieved. The MQW VCSEL was dominated by nonlinearities due to carrier population at duty cycles of 10% or less causing the VCSEL to blueshift. A nonlinear relationship is shown between input power and output power and is attributed to the optical Kerr effects in the mirror layers and gain region. Finally, broad spectrum reflectivity plots are generated indicating uniformity of the VCSEL fabrication.

Characterization of Nonlinear Effects in

Optically Pumped

Vertical Cavity Surface Emitting Lasers

I. Introduction

This thesis explores the nonlinear effects in optically pumped Vertical Cavity

Surface Emitting Laser⁺ ‚ CSELs). VCSELs are a relatively new type of

semiconductor laser that have the potential for many applications--some of which have

not been fully explored. This research is significant in that it opens the door to

possible application of VCSELs using nonlinear phenomena. Some examples of these

applications include "quasi" Q-switched VCSELs and optical switches.

1.1 Background

The family of semiconductor lasers have many advantages over chemical, gas,

and solid state lasers in that they are much smaller, require less power to operate, have

much higher efficiency (up to 40 - 60%), and have higher reliability. There are two

basic types of semiconductor lasers--edge emitting and surface emitting. Both types

are made of the same basic materials and are fabricated in similar ways, but it is

primarily the architecture which differentiates the two types of lasers. A Vertical

Cavity Surface Emitting Laser (VCSEL) is a semiconductor laser that lases out of the

top of the wafer and the more common edge emitting laser lases out of the edge of the

wafer. The VCSEL architecture has some significant advantages over edge emitting lasers. First, VCSELs can be made to lase in one longitudinal mode--desirable for communications purposes. Second, VCSELs can potentially be produced in an array of up to 1 million VCSELs on a 1 cm^2 chip [13:638]. Such a laser array would have many applications due to the close proximity of the VCSELs and their efficiency.

1.1.1 VCSEL Architecture

As seen in Figure 1.1, the cavity of the VCSEL is formed vertically and the mirrors (Distributed Bragg Reflectors--DBR) are grown monolithically on the substrate material. These mirrors can be designed to reflect 99% of the light (as opposed to edge emitting lasers which usually use the 32% reflection of the material/air interface [13:621]). The high reflectivity for VCSELs is necessary in part to compensate for the short cavity length ($\sim$1μm) versus $\sim$300μm for edge emitters.
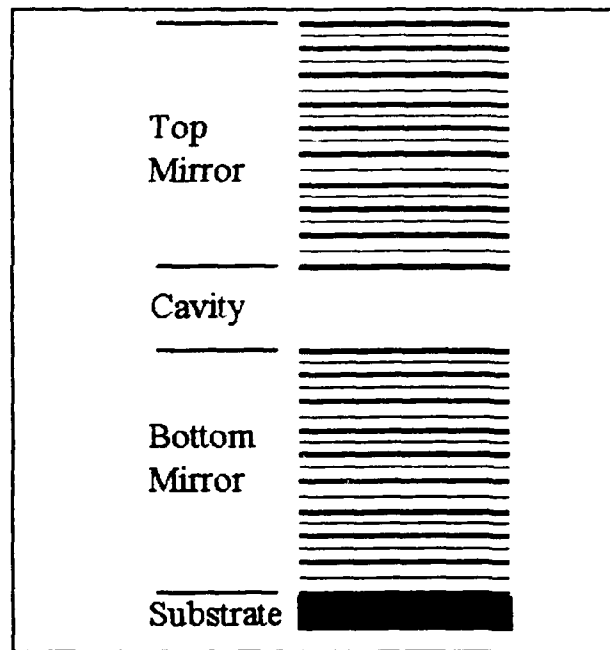
Figure 1.1. VCSEL architecture

1.1.2 Nonlinearities of VCSELs

Despite their advantages, VCSELs (and edge emitters) have a characteristic which is generally considered undesirable. The

semiconductor materials comprising the gain region and mirrors of VCSELs (e.g., GaAs, AlGaAs) are nonlinear in that their indices of refraction change during operation due to temperature change within the cavity, carrier population, and intensity of the lasing field. Refractive index changes modify the output amplitude and wavelength of the VCSEL. However, if properly designed, a VCSEL could make use of these nonlinearities. Nonlinear optical switches have already been made using the wavelength dependence on injected current, and there is the potential to make a quasi Q-switched VCSEL using the same nonlinear shift phenomenon. However, for Q-switching to work it must be the lasing field directly which spoils the cavity. Spoiling the cavity means moving the longitudinal mode out of the reflection envelope associated with DBR Fabry-Perot etalons (see Figure 2.2).

In order to propose a construction for a Q-switched VCSEL we must fully understand the effect temperature, carrier injection, and lasing field have on the output wavelength. Various articles have presented mathematical models for the changes in absorption of the VCSEL *materials* due to these three factors. However, how these factors combine to change the characteristics of VCSELs is not entirely known. In addition, most of the articles on this subject deal with electrically pumped VCSELs which, because of the joule heating effects of electrical pumping, focus on temperature effects. As a result, there may be a gap in understanding the nonlinear effects in VCSELs concerning carrier injection and internal field.

1.2 Problem Statement

This thesis seeks to quantify the shift in wavelength and change in output amplitude as a result of different optical pump configurations. Specifically, VCSEL output characteristics will change as a result of changes in the index of refraction and changes in the cavity length, and it is desirable to know how these changes are effected by the pump configuration and the VCSEL architecture.

1.3 Scope

It is assumed that the reader has a basic understanding of the semiconductor theory and VCSEL operation. However, even with a good background in these areas the variety, competition, and interdependence of the nonlinear mechanisms, combined with the limitations of the laboratory configuration make *modeling* a VCSEL response nearly impossible and certainly beyond the scope of this effort. However, armed with the theory of VCSEL operation and semiconductor nonlinearities it will be possible to qualitatively explain the results obtained.

1.4 Approach

This research looks to quantify the contribution of temperature change, carrier population, and internal field effects to the change in index of refraction. For the greatest flexibility in operation of the VCSEL we will optically pump it. Optical pumping has advantages other than flexibility; the most important of which is that it avoids joule heating and the complex fabrication processes associated with electrically pumping. Disadvantages include complexity of the laboratory setup, difficulty in

reproducing results, results which are dependent on pump wavelength, and a setup which precludes practical application.

Still the optical pump configuration is the first step in characterizing a VCSEL. We will demonstrate that by pulsing the pump, VCSEL nonlinearity due to cavity temperature can be reduced to the point that the nonlinear effects due to carrier population dominate. It will be shown that field effects appear to be minimal and are not likely to provide the wavelength shift required to Q-switch.

The laboratory setup permits reflectivity analysis of the VCSEL, as well as imaging capability. Reflectivity measurements are made using a low intensity broadband source to illuminate the VCSEL. The reflected energy is recorded and analyzed spectrally.

II. Theory

A VCSEL is characterized by its gain and the lasing wavelength. Both characteristics are determined by the architecture of the semiconductor material and as such are subject to nonlinear changes. All optical nonlinearities in VCSELs can be thought of as changing the absorption (or gain) and as a result, the index of refraction through the Kramers-Kronig relations [14:179]. It is useful to divide the mechanisms causing the nonlinearity into two groups--one affecting the net gain and the other the lasing wavelength. Net gain is affected by changes in the bandgap due to heating, changes in the reflectivity of the mirrors due to index of refraction changes and thermal expansion, and changes in carrier population. The lasing wavelength is affected by changes in the cavity length and refractive index changes due to free carrier injection, internal lasing field, and thermal properties. It is necessary to understand that these mechanisms are not mutually exclusive. For example, carrier population affects the gain profile as well as the longitudinal mode location.

In the following sections, the concept of absorption is reviewed and then each of the nonlinear mechanisms will be discussed followed by an analysis of how they act together. Finally the theory will be extended to MQW lasers.

2.1 Absorption and Index of Refraction

Absorption is defined in general terms as the relative rate of decrease in light intensity in the direction of propagation. In semiconductor materials the fundamental absorption is given by,

$$\alpha\,(h\nu)\ =\ A\sum P_{if}n_i n_f \qquad \bullet \qquad (2\text{-}1)$$

where P_{if} is the probability that a transition will occur from the initial to the final

state, n_i and n_f are the density of states, and A is a factor involving selection rules

[12:35]. The quantity $P_{if}n_i n_f$ is summed over all transitions having energy $h\nu$. The

minimum energy at which a photon will be absorbed, $h\nu_0$ (at 0°K), defines the

minimum bandedge or bandgap. At room temperature, the bandedge will smear and

permit absorption of energy less than $h\nu_0$.

Any change in absorption can be represented as a change in refractive index

using Kramers-Kronig Relations [14:179]. The development of Kramers-Kronig

relations begins with the complex susceptibility of dielectric materials given by,

$$\chi\ =\ \chi'\ +\ j\chi'' \qquad (2\text{-}2)$$

where χ' and χ'' are the real and imaginary susceptibility respectively. Eventually it

can be shown that the index of refraction, n, and absorption are related to

susceptibility by,

$$n\ -\ j\frac{\alpha}{2k_o}\ =\ (1\ +\ \chi'\ +\ j\chi'')^{1/2} \qquad (2\text{-}3)$$

where α is absorption, k_o is the wavenumber in free space. Kramers-Kronig relations

(seen on the next page) relate χ' and χ'' so that a change in one (e.g., absorption)

results in a change in the other (e.g., refractive index) [14:179]. Equations 2-3, 2-4,

and 2-5 can be combined to yield Equation 2-6 where P is the Cauchy principal value

2-2

$$\chi'(\nu) = \frac{2}{\pi} \int_0^\infty \frac{s\chi''(s)}{s^2 - \nu^2} ds \qquad (2\text{-}4)$$

$$\chi''(\nu) = \frac{2}{\pi} \int_0^\infty \frac{\nu\chi'(s)}{\nu^2 - s^2} ds \qquad (2\text{-}5)$$

$$n(E) = 1 + \frac{hc}{2\pi^2} P \int_0^\infty \frac{\alpha(E')}{E'^2 - E^2} dE' \qquad (2\text{-}6)$$

of the integral above, h is Planck's constant, and c is the velocity of light [16:356].

Note that not all changes to the refractive index are nonlinear. Doping changes the index of refraction in that the absorption increases near the bandedge. The increase is exhibited as a shoulder in the absorption spectra and is fairly localized (spectrally) due to the low concentration of the impurity [12:64]. This effort does not address the refractive index change due to doping.

2.2 Change in Gain

Changes in the gain of a VCSEL can be considered changes in the index of refraction if one regards changes in gain as changes in negative absorption. The basic unsaturated net gain equation for a VCSEL is given by,

$$G = \Gamma g - \alpha - \frac{1}{L} \ln\left(\frac{1}{r_1 r_2}\right) \qquad (2\text{-}7)$$

where Γ is the confinement factor, g is the optical gain, α is the scattering losses, L is the length of the cavity, and r_1 and r_2 are the reflectivities of the mirrors [4:1613] (the last factor is the mirror losses per unit length). The optical gain (or gain coefficient) is given by Saleh as

$$g(v) = \frac{\lambda^2}{8\pi\tau_r} \varsigma(v) f_g(v) \qquad (2-8)$$

where $\varsigma(v)$ is the density of states, τ_r is the recombination lifetime, and $f_g(v)$ is the Fermi inversion factor [14:611]. The Fermi inversion factor depends on the quasi-Fermi levels, temperature, and population of free carriers and is given by,

$$f_g(v) \equiv f_c(E_2) - f_v(E_1) \qquad (2-9)$$

where f_c is the Fermi function for the conduction band at energy E_2 and f_v is the Fermi function for the valence band at energy E_1. The quasi-Fermi energy levels, E_1 and E_2, are given by,

$$E_1 = E_v - (3\pi^2)^{2/3} \frac{\left(\frac{h}{2\pi}\right)^2}{2m_v} \rho^{2/3} \qquad (2-10)$$

$$E_2 = E_c + (3\pi^2)^{2/3} \frac{\left(\frac{h}{2\pi}\right)^2}{2m_c} \eta^{2/3} \qquad (2-11)$$

where E_c and E_v are the conduction and valence bandedge energies respectively, m_c and m_v are the effective mass of the electrons and holes, and η and ρ are the electron

2-4

and hole populations (at $0°K$). Finally, the temperature dependance can be seen in the Fermi function which is given by,

$$f(E) = \frac{1}{\exp[(E - E_f)/k_B T] + 1} \qquad (2-12)$$

where E_f is the Fermi level, k_B is Boltzmann's constant, and T is the temperature in Kelvin. Equations 2-10, 2-11, and 2-12 show that the gain is directly affected by carrier populations and temperature. An increase in temperature will increase the quasi-Fermi levels, decreasing the population near the bandgap and decrease the gain.

Figure 2.1 [14:613] illustrates the effect of carrier injection on the gain profile. As carrier concentration increases, the gain increases (as predicted by (2-10) and (2-11) above), and the peak of the gain curve blueshifts (i.e., moves to shorter wavelengths) as a result of the quasi-Fermi levels separating.
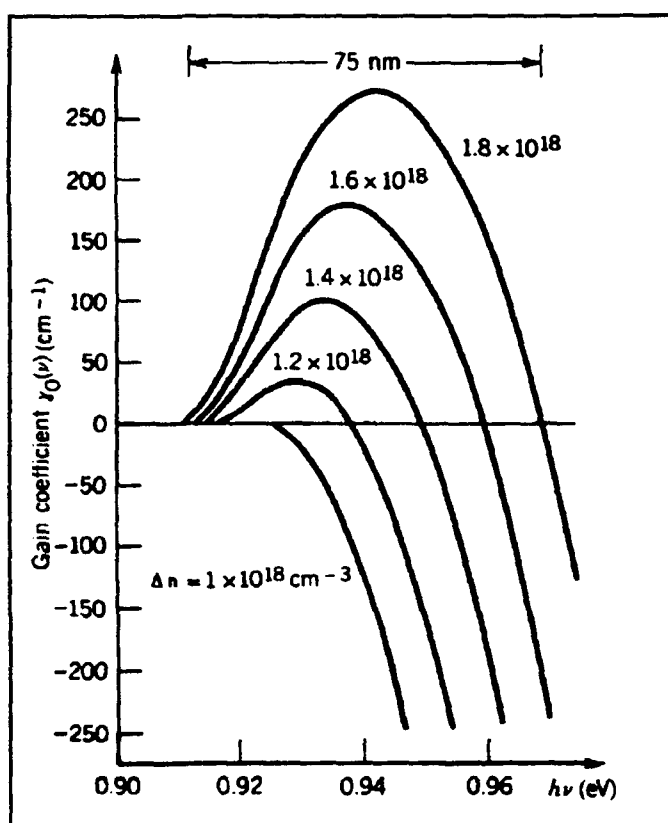
Figure 2.1. Calculated gain coefficient for an InGaAsP laser amplifier versus photon energy. The different traces represent different carrier concentration.

2.2.1 Changes in Bandgap

The active region (i.e., the cavity) of a VCSEL is typically on the order of $1 - 3\mu m$

and can generate up to milliwatts of power [11:128]. The output power is of course the result of electron-hole recombinations. However, most of the electron-hole pairs generated within the cavity recombine nonradiatively (i.e., not producing a photon) and instead produce phonons leading to lattice heating [13:XI-7]. Changes in the lattice spacing will change the bandedge, changing the absorption, and the index of refraction. In AlGaAs and GaAs, as in most materials, the change in temperature causes a shift of the absorption spectrum to lower frequencies (i.e., the bandgap narrows) according to the following equation:

$$E_g(T) = E_g(0) - \frac{\alpha T^2}{T + \beta} \qquad (2-13)$$

$E_g(0)$ is the bandgap at $0°K$, T is temperature in Kelvin, β is a value close to the DeBye temperature, and α is a proportionality constant [16:14]. At room temperature, the direct gap energy dependence (dE/dT) of semiconductor materials is nearly linear and can be approximated by a dE/dT coefficient (e.g., -3.9×10^{-4} eV/K for GaAs, and -5.2×10^{-4} eV/K for AlAs) [16:16] (see Table 2.1). This means that as the temperature in the gain region increases, the output wavelength will tend to increase. For example, using the constants provided in Swaminathan we find that for a $7°C$ change in temperature the wavelength changes by 0.0002eV or 1.22Å.

2.2.2 **Reflectivity Changes** The mirrors of a VCSEL are parallel Distributed Bragg Reflectors (DBRs) and form a Fabry-Perot etalon. The reflectivity of the

mirrors are determined by the index of refraction of the layers, their thickness, and the

number of layers. The resulting

Fabry-Perot reflectivity is

plotted versus wavelength as

shown in Figure 2.2. As either

the index of refraction or layer

thickness change, the

reflectivity profile will change.

Referring to Equation 2-7 it is

easy to see that as the
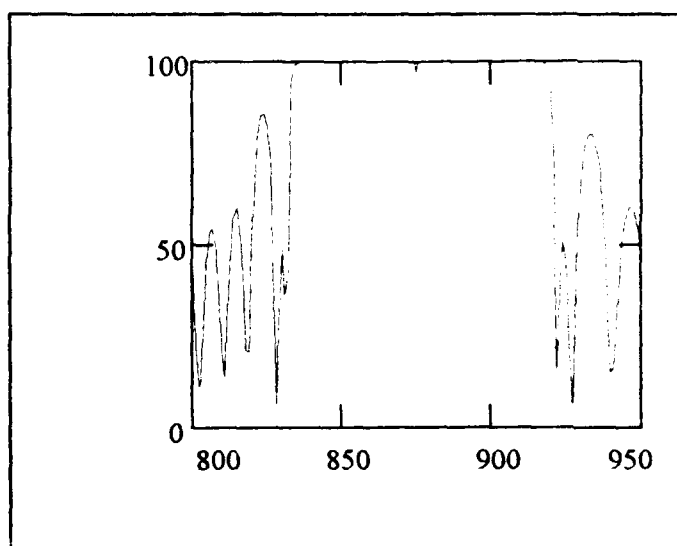
Figure 2.2. Calculated reflectivity for VCSEL operating at 875nm (architecture same as Old 3λ).

reflectivity decreases for a

given frequency, the losses in the

cavity will increase and net gain will

decrease. Figure 2.3 and 2.4 show

calculated VCSEL reflectivity as a

result of changing the index of

refraction of one mirror material by

10% higher and lower [2:Append A].

The result is that the high reflectivity

Figure 2.3. Calculated reflectivity with the refractive index of the high index mirror layer increased by 10%.

envelope has shifted to the point at

which it just supports the 875nm

lasing frequency. A larger change in the index of refraction could move the 875nm
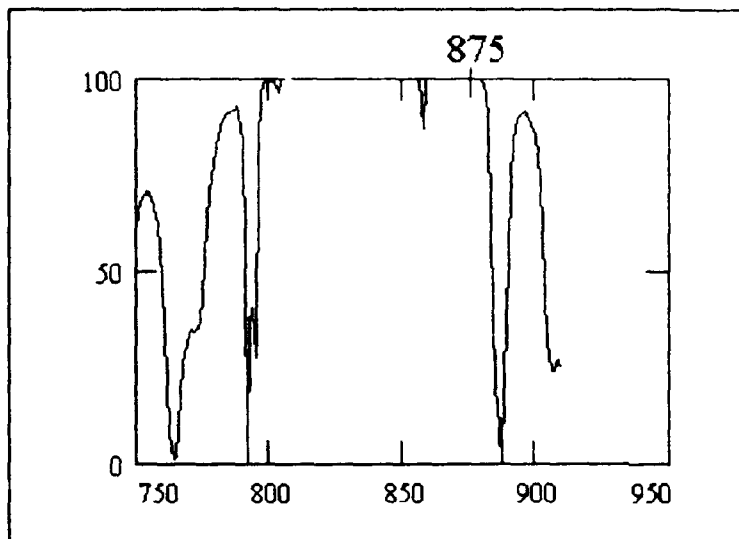
Figure 2.4. Calculated reflectivity with the refractive index of the high index mirror layer decreased by 10%.

longitudinal mode out of the high reflectance zone, and lasing would stop

2.3 Longitudinal Mode Movement

Within the high reflectivity envelope of the Fabry-Perot etalon is a single longitudinal mode (represented by a dip in the reflectivity of the envelope called the Fabry-Perot dip), which is of course determined by the optical path length of the cavity (additional longitudinal modes exist but they are separated by a distance determined by Equation 2-14 and outside the high reflectivity envelope). The longitudinal mode will shift with changes in the index of refraction and cavity length. The wavelength of this mode is given by,

$$\lambda = \frac{2nd}{m} \qquad (2\text{-}14)$$

where d is the cavity length and m is the order of the mode. Here it is easy to see that as n or d increase λ must increase. d changes with temperature as dictated by the coefficient of expansion. n changes due to several nonlinear factors: temperature properties, injected carriers, and internal field effects.

2.3.1 **Expansion Coefficient**   As with most materials, GaAs and AlAs (as well as AlGaAs and InGaAs) increase in length as temperature increases The coefficient of thermal expansion (α_{exp}) for GaAs, AlAs, and AlGaAs are given in Table 2 2 For example, referring to Equation 2-15, a change in cavity temperature of $100^{\circ}C$ in a 3λ

$$\Delta l = \alpha_{exp} l \Delta T \qquad (2\text{-}15)$$

VCSEL would increase the cavity length by almost 2nm and the lasing wavelength by 0.6nm to 860.6nm (see Equation 2-14) Another factor that affects the temperature characteristics of a VCSEL is thermal conductivity If VCSEL operation is pulsed, the temperature increase in the cavity will be permitted to dissipate while the pump is off, reducing the temperature gradient Thermal conductivity for GaAs is 0.46 W/cm/K and it is possible to calculate the time required to dissipate a local temperature increase (e.g., in the cavity) to the surrounding substrate using this heat transfer equation,

$$H = -kA\frac{dT}{dx} \qquad (2\text{-}16)$$

where H is the heat flow rate (joules per second), k is the thermal conductivity, A is area, and dT/dx is the temperature gradient [6:358]   However, the time required to dissipate cavity heat is more easily determined experimentally--$1\mu s$ is used by Hasnain [7:1381] Also important is the time required for the length and index to change due to heating For GaAs the pulse width should be less than 100ns (50ns @ $1\mu s$ is used by Hasnain [7:1381]).

Table 2.1. Values for selected properties of GaAs, AlAs, and AlGaAs

Material	$n^{\#}$ @ (27°C) $(E \approx E_g)$	Bandgap** (eV)	dE/dT^* (direct gap) $(\times 10^{-4} eV/°C)$	dn/dT^{***} $(\times 10^{-4}/°C)$
GaAs	3.6	1.424	-3.9	1.34
AlAs	3.2	2.168	-5.2	---
$Al_xGa_{1-x}As$	$\approx 3.6 - 0.4x$	$1.424 + 1.247x$ $(0 \le x \le 0.45)$ $1.9 + .125x + 1.43x^2$ $(0.45 \le x \le 1.0)$	---	---

#[14:588], *[16:15], **[1:R3], ***[9:1399]

Table 2.2. Values for thermal properties of
GaAs, AlAs, and AlGaAs.

Material	Thermal* Conductivity (W/cm/C)	Thermal Expansion Coefficient** $(\times 10^{-6}/°C)$
GaAs	0.46	6.4
AlAs	0.8	5.2
$Al_xGa_{1-x}As$	---	$6.4 - 1.2x$

*[16:15], **[1:R3]

2.3.2 Refractive Index Changes There are three nonlinear mechanisms that affect the refractive index in semiconductor materials--temperature, carrier population, and the internal lasing field.

2.3.2.1 Thermal Effects The thermal effects of concern here have already been discussed in Section 2.2.1. The change in temperature affects the lattice spacing, therefore the bandgap, and consequently the index of refraction. As

mentioned earlier, the bandgap varies linearly near room temperature, and since the bandgap and the index of refraction are directly related, the index of refraction varies linearly with temperature, dn/dT. See Table 2.1 for values of dn/dT.

2.3.2.2 Injection of Carriers The steady state population of injected carriers is proportional to the intensity of the pumping medium [10:1745] and is given by Equation 2-17, where n_e is free carrier density, N_o is the initial free-carrier density,

$$\frac{n_e(n_e - N_o)}{N_o} = \frac{\alpha \tau_L 2\pi}{\hbar \omega} I \qquad (2\text{-}17)$$

α is the absorption coefficient, ω is the incident angular frequency, I is the irradiance of the radiation (W/m^2), and τ_L is the recombination time of the generated free carriers [9:1399]. Calculation of (2-17) is not straight forward as τ_L is itself a function of carrier population and temperature, and α is a function of many mechanisms as evidenced by this document.

There are four primary phenomena related to the injection of carriers that affect the index of refraction: bandfilling, bandgap shrinkage, free-carrier absorption, and plasma screening.

• *Bandfilling* results when carriers fill the lower levels of the conduction band. As a result, the energy required to get an electron into the conduction band increases, blueshifting the absorption spectrum (i.e., moves to shorter wavelengths). The change in absorption is given by [3:115],

$$\Delta\alpha\,(N,\,P,\,E) \;=\; \frac{C_{hh}}{E}\sqrt{E - E_g}\,[\,f_v(E_{ah}) \;-\; f_c(E_{bh}) \;-\; 1\,]$$

<div align="right">(2-18)</div>

$$+\;\frac{C_{lh}}{E}\sqrt{E - E_g}\,[\,f_v(E_{al}) \;-\; f_c(E_{bl}) \;-\; 1\,]$$

where: N is the number electrons,
P is the number of holes,
E is the incident energy,
E_g is the band gap energy with no injection,
E_{ah} is the energy in the valence band corresponding
    to heavy holes,
E_{al} is the energy in the valence band corresponding
    to light holes,
E_{bh} is the energy in the conduction band
    corresponding to heavy holes,
E_{bl} is the energy in the conduction band
    corresponding to light holes,
C_{hh} is a fitting constant for the heavy holes,
C_{lh} is a fitting constant for the light holes,
f_c is the Fermi function for the conduction band (2-10),
f_v is the Fermi function for the valance band (2-11).

Without fully explaining Equation 2-18, it is enough to see from the Fermi

functions (Equations 2-10 and 2-11) that as the carrier level increases, the Fermi levels

increase decreasing the absorption coefficient. This is the same phenomena which

caused the gain profile to blueshift. Using Kramers-Kronig relations, Bennett shows

that as carrier concentration increases the index of refraction decreases below the

bandedge and increases above it [3:118].

• *Bandgap shrinkage* or bandgap renormalization results from injected carriers filling

the lower states of the conduction band first. The Coulomb forces existing between

the excited carriers tends to repel each other, effectively screening the electrons and

lowering the energy of the bandedge given by,

$$\Delta E_g(\chi) = \frac{\kappa}{\epsilon_s}\left(1 - \frac{\chi}{\chi_{cr}}\right)^{1/3} \qquad \chi \geq \chi_{cr} \qquad (2\text{-}19)$$

where κ is a fitting constant, ε_s is the relative static dielectric constant of the semiconductor, χ is the concentration of free electrons or holes, χ_{cr} is the critical concentration of free carriers [3:117]. As the description of this phenomena predicts, the absorption and the index of refraction increase at just below the bandedge, thus lowering the bandedge.

• *Free-carrier absorption*, also known as the plasma effect, is described as absorption of a photon resulting in an electron changing states *within* a band. This effect is in direct proportion to carrier concentration and the square of the wavelength given by,

$$\Delta n = -\left(\frac{e^2\lambda^2}{8\pi^2 c^2 \epsilon_o n}\right)\left(\frac{N}{m_e} + \frac{P}{m_h}\right) \qquad (2\text{-}20)$$

where N and P are the number of electrons and holes respectively, and m_e and m_h are the effective masses [3:117]. Equation 2-20 shows that the change in index of refraction will always be negative and will become more pronounced as the carrier concentration increases and/or the wavelength increases (i.e., free carrier absorption is greatest below the bandgap).

• *Plasma Screening* is a common nonlinear phenomenon which results from excitons screening. Excitons result from the Coulomb attraction of an electron in the

conduction band and a hole in the valence band. The effect of excitons is a reduction in the effective mass of the free electron [12:12], and results in a peak in the absorption spectra (called the exciton peak). However, the carrier levels in an operating VCSEL are sufficiently high levels that the inter-electron forces in the conduction band (see bandgap shrinkage) overpower the Coulomb force and the electron-hole pairs disassociate (i.e., the excitons ionize) and the exciton peak disappears [13:XI-2]. Therefore, plasma screening is not a significant effect in VCSEL nonlinearity.

Figure 2.5 shows the changes in absorption and index of refraction for bulk GaAs relative to the bandgap for different free carrier populations (all carrier nonlinearities described above are combined to yield the figure). It is easy to see that the nonlinearity is evident primarily near the bandgap and at high carrier levels [13:301]. The shoulder in trace #1 is the result of the exciton peak. As carrier levels increase, the shoulder disappears. Note: In Figure 2.5, E_g^o is the bandgap energy and E_R is the exciton Rydberg energy.

2.3.2.3 Lasing Field

Near the band edge, the lasing field depletes the available carriers effectively reducing the carrier lifetime (τ_L in (17)) and the carrier population. This reduction in carriers reduces the quasi-Fermi levels and redshifts the lasing frequency [14:123]. However, once lasing begins, the gain clamps to the loss line and any remaining refractive index change is due to third order effects.

The third order nonlinear effect results when the field within the cavity of the VCSEL is established subjecting the crystalline material to the high frequency electric
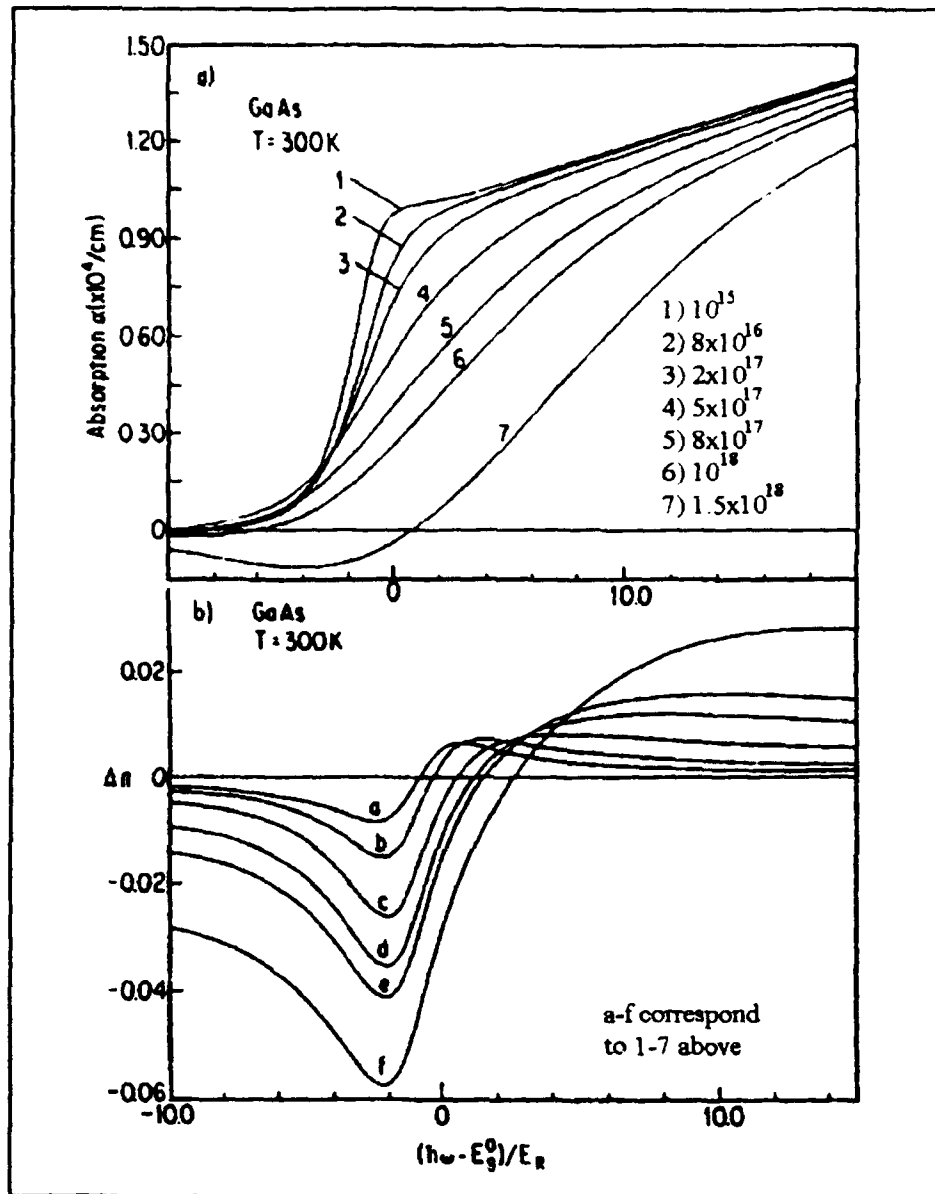
Figure 2.5. a) Calculated absorption spectra for different carrier populations (cm^{-3}); b) Δn from Kramers-Kronig relation.

field and causes an induced polarization to form according to the following Taylor

series expansion:

2-15

$$P_i = \epsilon_o \chi_{ij} E_j + 2 d_{ijk} E_j E_k + 4 \chi_{ijkl} E_j E_k E_l + \dots \qquad (2\text{-}21)$$

where P_i is the ith component of the instantaneous polarization, E_i is the ith component of the instantaneous field, and χ_{ijkl} is the third order susceptibility (or $\chi^{(3)}$). $\chi^{(3)}$ is determined by the magnitude of the E-field at frequency ω and the incremental change in the susceptibility ($\Delta\chi$). Semiconductor material is centrosymmetric and as such the second order term, d_{ijk}, is zero. As the third term in (2-21) indicates, third order nonlinear polarization is the result of the interaction of three optical fields. The interaction of an electromagnetic field with an atomic transition is accompanied not only by absorption of energy but also by a dispersive effect in which the phase velocity of the incident wave depends on the frequency. The reason is that when the frequency of the wave is near that of the atomic transition, the atoms acquire large dipole moments that oscillate at ω and the total radiated field is now the sum of the incident field and the field radiated by the dipoles [15:100]. Therefore, the index of refraction of the semiconductor material changes as the internal field is established.

2.3.2.4 Interaction of Effects

The effects of carrier injection, temperature, and lasing field have been presented as though their contribution to the change in refractive index is mutually exclusive. This is not the case. For example, it is easy to see that above threshold, an increase in pump intensity would increase carrier concentration, as well as, field intensity and cavity temperature. Isolating and

characterizing each effect is difficult and will depend greatly on an effective laboratory procedure.

2.4 Overall Actions

During operation a VCSEL will produce a given wavelength at a given power. Depending on the lasing spot, the output can be steady in both wavelength and amplitude, or it may vary. Of the mechanisms discussed, only the thermal effects would vary at a rate one could see without the use of significant diagnostic equipment (e.g., an autocorrelator). As temperature is introduced into the system, the cavity length and index of refraction will change which may cause the VCSEL to stop lasing. If the VCSEL stops lasing, it will cool and as each parameter returns to normal, lasing may begin again. Table 2.3 shows some of the tendencies of an electrically pumped edge emitting laser as a function of substrate temperature. Note that threshold current is highly dependent on temperature. Most literature published on VCSELs concerns

Table 2.3. Typical performance of GaAs injection laser at $I = 2I_{th}$ for two different temperatures.

T ($^\circ$K)	I_{th} (A)	P_{in} (W)	I^2r (W)	P_{out} (W)	P_d (W)	η_p %	η_{ext} %
77	1	3.2	0.2	0.75	2.5	23	25
300	20	136	80	8.4	127.6	6.2	15

I_{th} - threshold current P_{out} - power out
P_{in} - input power P_d - dissipated power
I^2r - joule losses η_p - power efficiency
       η_{ext} - external quantum efficiency

*[12:234] data provided is that for an electrically pumped edge emitting laser

electrically pumped VCSELs. Electrically pumped VCSELs have the additional Joule

heating factor effecting their performance. This I^2R loss occurs when the DC electric current passes through the mirrors. Optically pumping the VCSEL avoids this phenomenon. Still, even in optically pumped VCSELs heat is the primary factor in refractive index change. From Table 2.1 we see that dn/dT is on the order of 10^{-4}, two orders of magnitude bigger than the thermal expansion coefficient. If we assume that the longitudinal mode shift is due only to thermal refractive index change then it is possible to determine the cavity temperature--in effect, use the mode shift as a thermometer. Table 2.4 provides a summary of the nonlinear actions in a VCSEL.

2.5 Multi-Quantum Wells

Multi-Quantum Well (MQW) VCSELs have distinct advantages over VCSELs with gain regions made of bulk material. The most important advantage is lower threshold current. Yet, for the most part, the nonlinear mechanisms described above affect MQW VCSELs in the same manner and degree. Some of the subtle differences include weaker Coulomb interaction due to the restricted dimensions of the gain region. A factor called phase filling becomes evident because the efficiency of screening is reduced and the phase space is more readily filled. Phase filling tends to blueshift the spectra. In addition, steps in the absorption spectra are evident and result from the discrete steps in the density of states.

Table 2.4. Summary of nonlinear mechanisms, actions, and effects. Action and Effect describe what happens to the output of the VCSEL as a consequence of the associated Mechanism increasing ($\uparrow$).

Mechanism	Action (assume mechanism $\uparrow$)	Effect (assume mechanism $\uparrow$)
Gain		
Bandgap (thermal $\uparrow$)	Bandgap decreases	decrease gain
Carrier population	Quasi-Fermi levels increase	increase and blueshift gain
Reflectivity	Losses decrease	increase net gain
Mode location		
Thermal expansion	Cavity length increases	redshift
Thermal index change	Index of refraction increases	redshift
Carrier population*	n $\downarrow$, below bandedge at $N=P=3\times10^{18}/cm^3$	blueshift
-band filling	n $\downarrow$, below bandedge at $N=P=3\times10^{18}/cm^3$	blueshift
-bandgap shrinkage	n $\uparrow$, below bandedge at $N=P=3\times10^{18}/cm^3$	redshift
-free carrier absorption	n $\downarrow$, below bandedge at $N=P=3\times10^{18}/cm^3$	blueshift
-plasma screening	no action below bandedge	---
Internal Field	reduces carrier τ_L, narrowing the quasi-Fermi levels; $\chi^{(3)}$ effect not considered	redshift

*[3:118]

III. Approach and Methodology

This section outlines the type of data required to fully characterize the nonlinearity of a VCSEL and how that data should be obtained. This section does not necessarily deal with practical considerations or physical constraints.

3.1 Methodology

Each nonlinear mechanism considered in Chapter 2 can be isolated and quantified using different experimental procedures. These procedures include varying the pump power, pulsing the pump, and operating the VCSEL both above and below threshold. Table 3.1 lists the four basic experiments required to characterize the nonlinear response of a VCSEL. Experiments #1 and #2 look at the response of the VCSEL below threshold. Without the VCSEL lasing, the internal field is not established and therefore any changes in λ are not due to changes in the internal field. In Experiment #1 the dominate effect will be heating because the VCSEL is pumped continuous wave (CW). For Experiment #2, cavity heating is reduced by pulsing the pump at pulse widths of less than 100ns at a rate of less than 1MHz (Note: Since the 100ns/1MHz limit was established for electrically injected VCSELs, we assume that it will be more than sufficient for optically pumped VCSELs). The resulting shift in λ will be dominated by carrier nonlinearity. The difference in λ shift between Experiments #1 and #2 will be due to heating of the cavity. Experiments #3 and #4 introduce lasing field to the equation. #3 will show the greatest λ shift since both cavity heating and lasing field contribute to redshift the spectrum.

Table 3.1. Ideal experimental procedures for isolating nonlinear VCSEL characteristics

#	Sub Temp	Pump: (width) (freq)	Input: (peak) (avg)	Lase?	Amp out	Analysis
1	const	cw	vary vary	no	N/A	λ change due to cavity temp, and injected carriers.
2	const	pulse =100ns =1MHz	vary vary	no	N/A	λ shift due to injected carriers
3	const	cw	vary vary	yes	free	λ and amplitude change due to cavity temp, lasing field, and injected carriers.
4	const	pulse =100ns =1MHz	vary vary	yes	free	λ and amplitude change due to injected carriers and lasing field.
OPTIONAL						
5	vary	cw	const const	no	N/A	λ change due to substrate temp, and cavity temp,.
6	vary	cw	const const	yes	free	λ and amplitude change due to changes in substrate temp, cavity temp, and lasing field.
7	vary	pulse =100ns =1MHz	const const	yes	free	λ shift due lasing field, and substrate temperature.

Finally, #4 will indicate the competition between injected carriers and lasing field, the dominant mechanism will cause λ to blue or redshift respectively.

In addition to the four basic experiments, Experiments #5, #6, and #7 explore the effects of varying the temperature of the VCSEL substrate. If the pump duty cycle (ratio of pulse width to time between pulses) remains constant then the temperature

gradient between the VCSEL cavity and the surrounding material should remain

constant. As a result, as the substrate temperature increases, the cavity temperature

also increases. It has been shown that the substrate temperature has a linear

relationship to output wavelength [5:2699]. The slope of the wavelength versus

substrate temperature line is not expected to be different whether the VCSEL is

operating below and above threshold. The reason is that if the temperature gradiant

stays constant, then changes in substrate temperature will have the same effect on

output wavelength whether the VCSEL is lasing or not.

IV. Setup and Procedure

The experimental setup and procedure used to obtain the data is as important as the data itself. This section not only examines laboratory setup but also the limitations of the configuration and how those limitations dictate different procedures to generate the necessary data.

4.1 The Setup

The experimental setup has been designed to permit several different system configurations to be run simultaneously. These configurations are imaging, white light, and spectral analysis using an Optical Multi-channel Analyzer (OMA) and a scanning Fabry-Perot etalon. Figure 4.1 shows the entire experimental setup used during the experiments. The following sections detail the major subsystems found in the configuration: pump, VCSEL, white light, imaging, and scanning Fabry-Perot. The specifications of the major components of the system are provided at the end of the chapter.

4.1.1 The Pump Subsystem

The VCSEL is pumped by a tunable Ti:Sapphire CW/Picosecond/Femtosecond laser which is itself pumped by an 30W Argon laser. Figure 4.2 shows the pump subsystem. The Ti:Sapphire laser is tunable from 700nm to 1000nm, although not contiguously. Three different mirror sets optimize the Ti:Sapphire for operation in short, mid, or long wavelengths. For this setup the middle wavelength mirror set is used which allowed the output wavelength of the Ti:Sapphire crystal to be varied from 800nm to 940nm. In addition, a different output
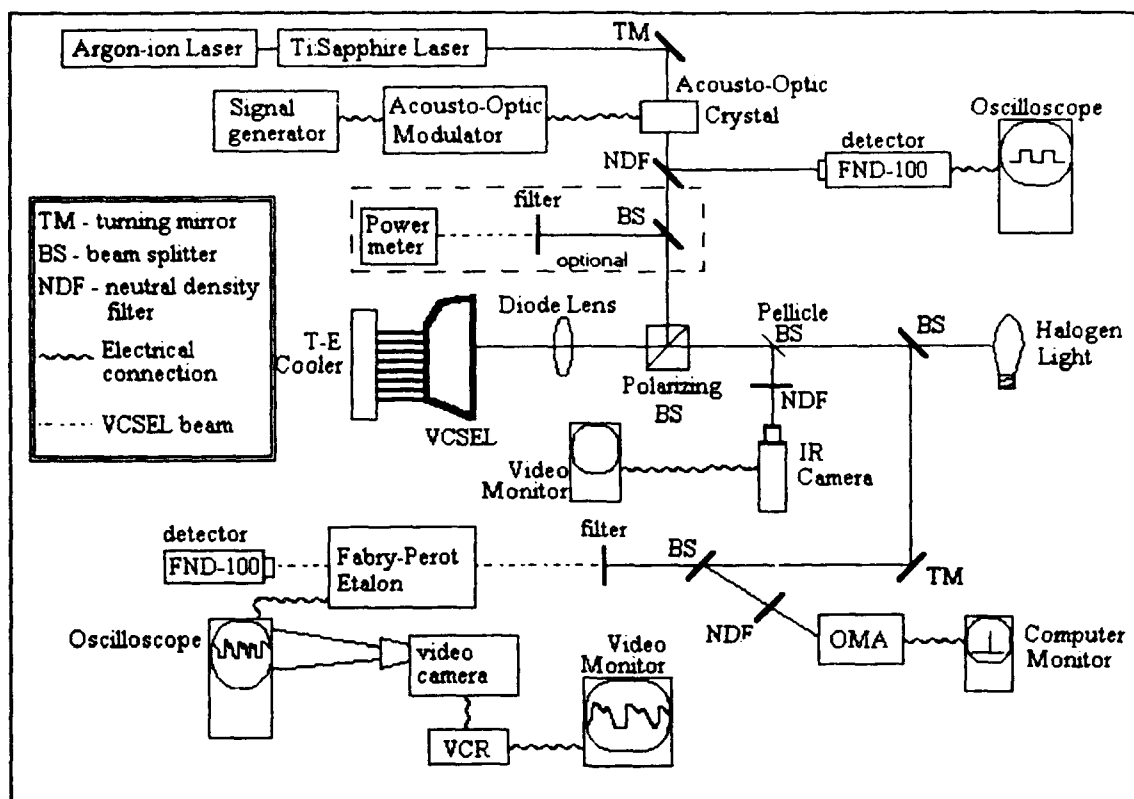
Figure 4.1. Laboratory configuration.

coupler and internal configuration was required for pico versus femtosecond operation.

We chose to run continuous wave (CW) or picosecond mode. In picosecond mode,

the output pulse width was approximately 1.5ps and the repetition rate was 76MHz

(the 76MHz determined by the internal cavity length of the Ti:Sapphire laser).
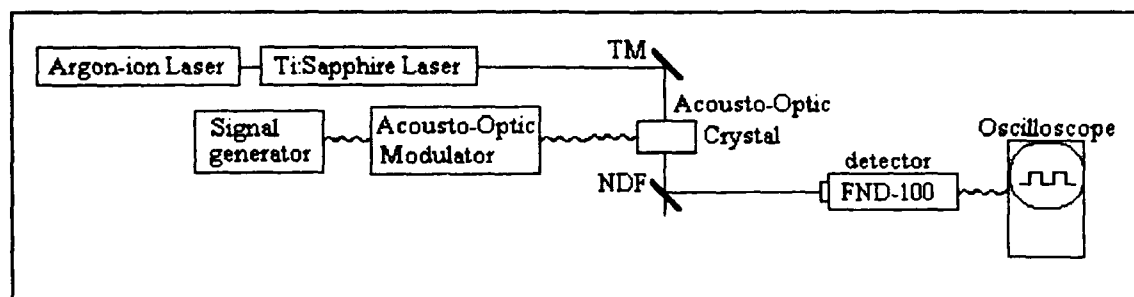
Figure 4.2. The pump subsystem.

The output beam of the Ti:Sapphire passes through an acousto-optic crystal. When activated, the associated acousto-optic modulator causes the acousto-optic crystal to deflect the incident beam into various orders, the number and intensity of which is determined by the amplitude of the modulating signal. In each order above (or below) zero, the beam is shifted in frequency by the 40MHz (the frequency of the modulating signal). Although the specifications state that conversion to the first order mode should be 85%, we were only able to achieve 25%. The lack of conversion is attributed to a poor mounting and adjusting fixture. Still, 25% conversion was sufficient to conduct nearly all conceivable experiments.

The frequency shift of the first order beam was not itself the reason for using the acousto-optic crystal. By using a signal generator, the 40MHz modulating signal was amplitude modulated causing the first order beam to be gated according to the output of the signal generator. Unfortunately, the crystal could not produce optical gate widths of less than about 200ns (FWHM). This is attributed to the "rise time" of the acousto-optic crystal which is 170ns.

The final aspect of the pump subsystem is a neutral density filter (NDF) which permits the intensity of the beam to be varied. The reflection off the NDF is detected by an FND-100 and displayed on an oscilloscope. The frequency response of the FND-100 could not reproduce picosecond pulses, but the detector *could* output a pulse train at 76MHz indicating that the Ti:Sapphire was operating in picosecond mode. By using the detector, non-intrusive monitoring of the pump signal was possible and all gate widths (FWHM) and repetition rates were measured using the associated oscilloscope.

There are four basic pump configurations used to pump VCSEL in this effort.

1) Continuous wave (CW), 2) gated CW--the CW pump is gated using the acousto-optic (AO) modulator, 3) picosecond, and 4) gated picosecond--picosecond gated with the AO modulator. In picosecond mode, the Ti:Sapphire could not produce an average power as large as in CW mode (which was as high as 3W). However, a picosecond beam with the same average power as a CW beam produced 8770 times the peak power. This transient photon surge into a VCSEL had some definite advantages which will be discussed later.

4.1.2 The VCSEL Subsystem The VCSEL subsystem holds the VCSEL secure, cools the VCSEL, gets the pump beam onto the VCSEL, and separates the VCSEL output from the reflected pump beam. This subsystem is also the heart of the entire configuration and as such has extensive alignment features.
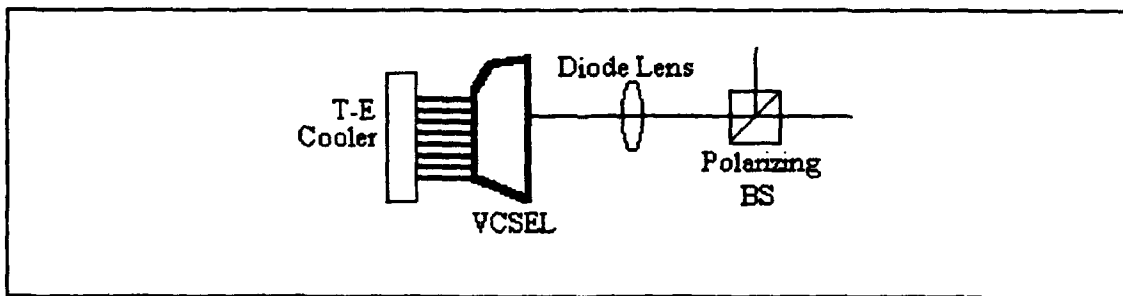

Figure 4.3.   VCSEL subsystem.

The pump beam enters the subsystem through a polarizing beam splitter which provides a 1000:1 extinction ratio for the non-transmitted beam. The output of the VCSEL passes back *through* the polarizing beam splitter provided the polarization of the VCSEL output is horizontal (see Figure 4.4). There also is a significant (20 - 30%) amount of the pump beam reflected off the VCSEL surface which is collinear
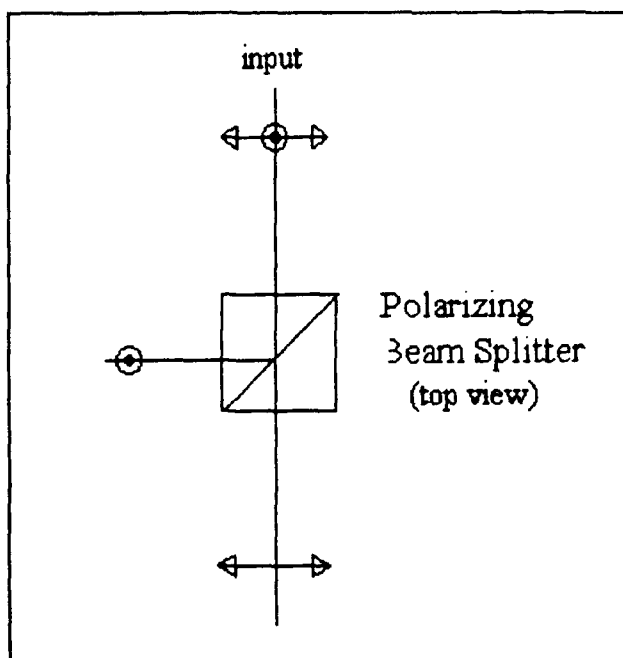
4-4

Figure 4.4. Polarizing beam splitter operation.

with the VCSEL output. However, because the polarization of the reflected pump beam remains vertical the polarizing beam splitter reflects it back toward the Ti:Sapphire laser. Use of the polarizing beam splitter dictates the polarization of the input and output beam, restricting some of the flexibility of this system.

The diode lens is a multiple lens set which provides diffraction limited performance in monochromatic applications. The lens used with this setup has a focal length of 14.2mm and a spot size of 1.85μm. The lens can be translated in X, Y, and Z (focus) as well rotated (or tilted) in X and Y. The VCSEL is mounted with silicone heat sink compound on an assembly which contains a thermal-electric (T-E) cooler which is itself epoxyed onto an X/Y translation stage. The translation stage has a tolerance of 2μm per division. The T-E cooler is limited to a maximum temperature of 35°C.

4.1.3 **The White Light Subsystem**   For reflectivity versus wavelength plots a broad spectrum white light source (a halogen light) is used to illuminate the VCSEL surface. Ideally the white light would be normally incident to the VCSEL surface, but because of the diode lens in the beam path, some rays are obliquely incident resulting

in less than optimal performance of the VCSEL's ¼λ thin film mirror. As a result, the

lens will broaden some of the spectral features of the reflectivity plot. However, use

of the lens does have an advantage in that it concentrates the white light to a very

small spot. As a result, the plot generated represents that of a specific spot and is not

an average reflectivity of the VCSEL surface. It is not known if the lens in the beam

path results in a better or worse reflectivity plot. The reflection from the VCSEL

surface is directed into the OMA. The OMA has a bandwidth of 75nm about a
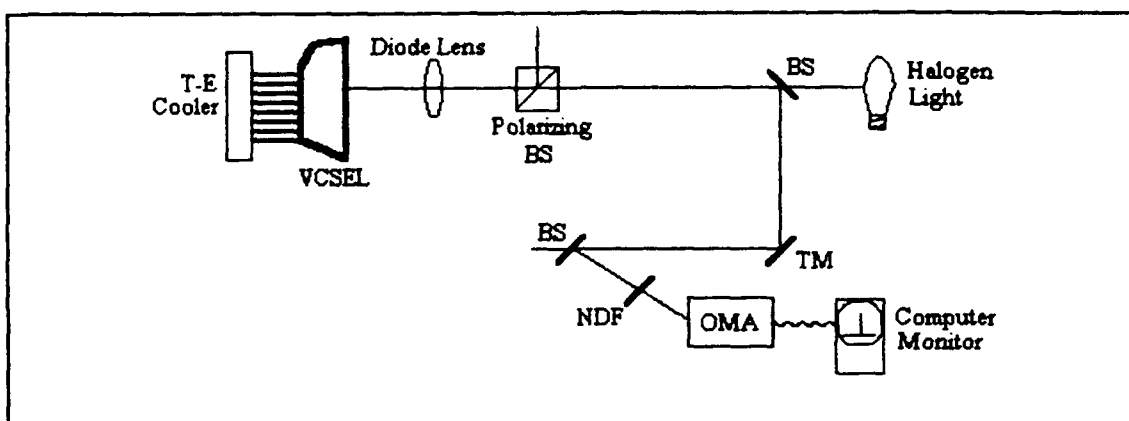

Figure 4.5. White light and OMA subsystem.

selectable center frequency and a resolution of 0.06nm. Reflectivity measurements

from the various center frequencies from 800nm to 975nm can then be combined into

a single plot (see Section 4.2).

The OMA is also used to display the spectral output of the lasing VCSEL. It

should be noted that the temporal response of the OMA was such that it could only

display the *average* spectral and intensity output.

4.1.4 **The Imaging Subsystem** The imaging subsystem serves two purposes.

First is to image the surface of the VCSEL using the white light and/or pump allowing

the physical surface to be viewed. This capability allows one to look for surface

irregularities and to ensure the white light and laser spot are coincident and properly

aligned. Imaging permitted the measurement of the laser spot (consistent with the
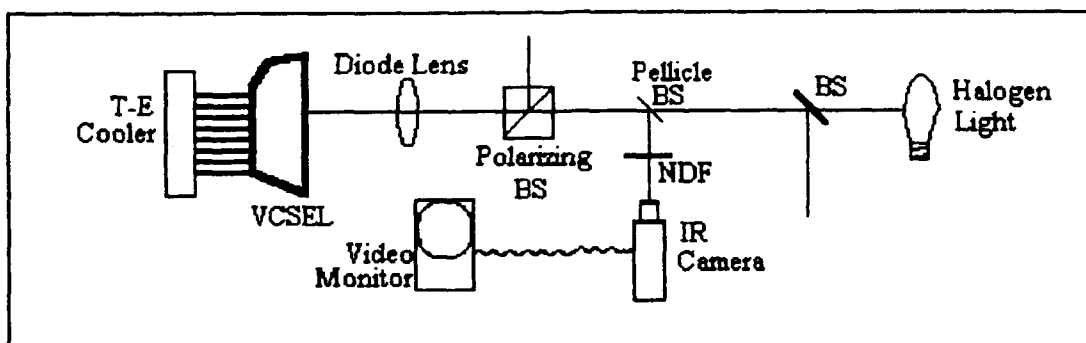

Figure 4.6. Imaging subsystem.

1.85μm specification) and the white light spot size--about 7μm. The spot size was

found by moving the spot past a feature on the VCSEL surface and noting the linear

translation (resolution on the translation stage is 1μm). Magnification is estimated to

be on the order of 10^4. Second, the imaging subsystem displays the VCSEL lasing

spot. The focus is different for imaging versus lasing; therefore the video monitor

does not show an *image* of a lasing spot rather a blurry spot which gets brighter when

the VCSEL is lasing.

4.1.5 **The Scanning Fabry-Perot Etalon Subsystem** The Scanning Fabry-Perot

(F-P) Etalon subsystem permits detailed analysis of the output VCSEL waveform in

two ways. First, the F-P is configured with a cavity length of 0.1363mm and a free

spectral range (fsr) of 1.1THz (±0.01THz). The resolution of the output waveform

(assuming a full fsr is displayed on the oscilloscope) is 0.06nm--the same as the OMA.

Less fsr would increased the resolution but the spectral width of the VCSEL output

was such that successive orders of the VCSEL output would overlap making analysis

impossible. Second, the scanning F-P allows better analysis of the VCSEL waveform

because the screen of the oscilloscope is imaged with a video camera and the image

recorded on a VCR. Measurements from the F-P can be made replaying the VCR in

slow motion. The input chromatic filter filters out the residual pump beam.

Because of the lack of additional resolution, difficulty of use, and of selecting

good, consistent data points, the Fabry-Perot etalon was not used greatly. Instead,
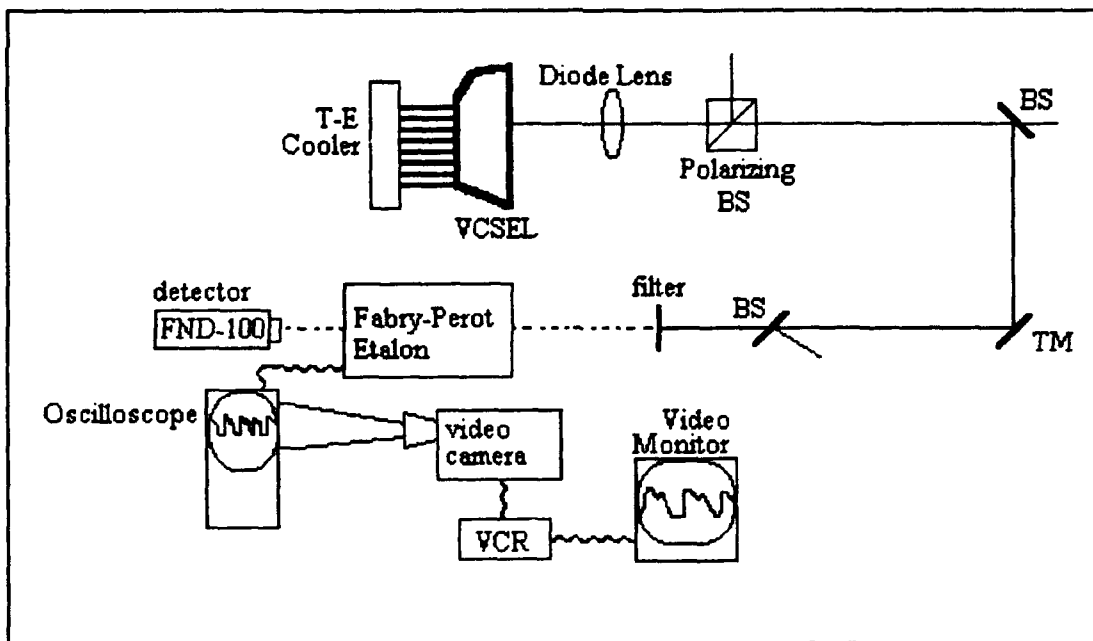

Figure 4.7. Scanning Fabry-Perot etalon subsystem.

because the experiments are only concerned with the general movement of the peak of

the VCSEL output, the OMA was sufficient.

4-8

4.2 The VCSELs

There were several VCSEL candidates from which to choose for this effort. The three chosen were, not surprisingly, the ones that lased. Two of the three have a gain region made from bulk GaAs material and the third uses InGaAs MQWs. Following are the VCSEL specifications along with sample reflectivity plots generated using the system described above. It should be noted that the reflectivity values only have a confidence of ±5% and are provided primarily to give an indication of the relative reflectivity of one wavelength versus another for a given VCSEL.

4.2.1 Old 3λ Bulk GaAs

This VCSEL was grown using Molecular Beam Epitaxy (MBE) technology in November of 1990 at the University of Arizona. As the title suggests, the cavity length is $3\lambda/n$ with λ being the design lasing wavelength of 875nm and n being the index of refraction of GaAs.

Material Parameters [2:5-3]:

    Number of layers for top mirror: 34
    Number of layers for bottom mirror: 45
    Active region: GaAs UGS (Uniform Gain Structure)
    Active region thickness: 0.726μm
    Substrate: GaAs
    Design wavelength: 875nm
    Low index layers: AlAs
    Calculated refractive index @ 875nm: 2.99573
    Physical layer thickness: 73.2nm
    High index layers: $Al_{0.127}Ga_{0.873}As$
    Calculated refractive index @ 875nm: 3.52773
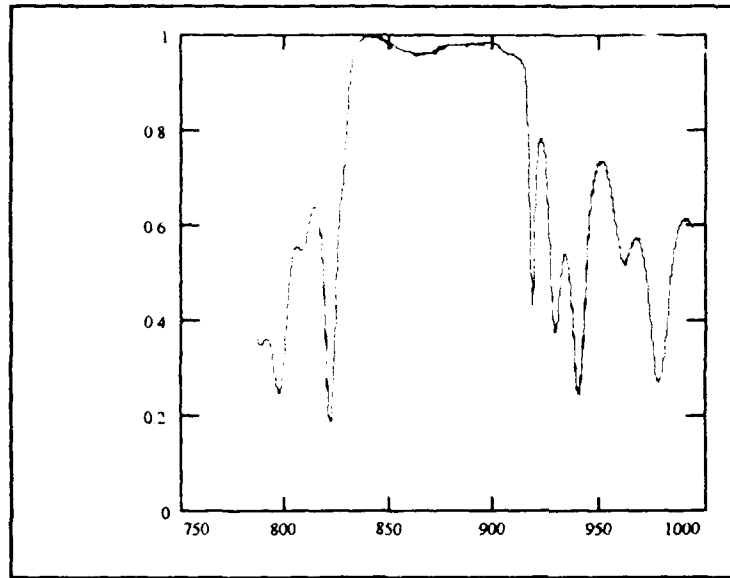   Physical layer thickness: 61.8nm

Figure 4.8. Old 3λ reflectivity plot.

4.2.2 New 3λ Bulk GaAs This VCSEL was grown using MBE in June of

1991 at the University of Arizona. It features the same basic architecture as Old 3λ

except the number of mirror layers are greater and therefore the reflectivity is

increased.

Material Parameters [2:5-7]:

        Number of layers for top mirror: 44
        Number of layers for bottom mirror: 51
        Active region: GaAs UGS (Uniform Gain Structure)
        Active region thickness: 0.726μm
        Substrate: GaAs
        Design wavelength: 875nm
        Low index layers: AlAs
        Calculated refractive index @ 875nm: 2.99573
        Physical layer thickness: 73.2nm
        High index layers: $Al_{0.127}Ga_{0.873}As$
        Calculated refractive index @ 875nm: 3.52773
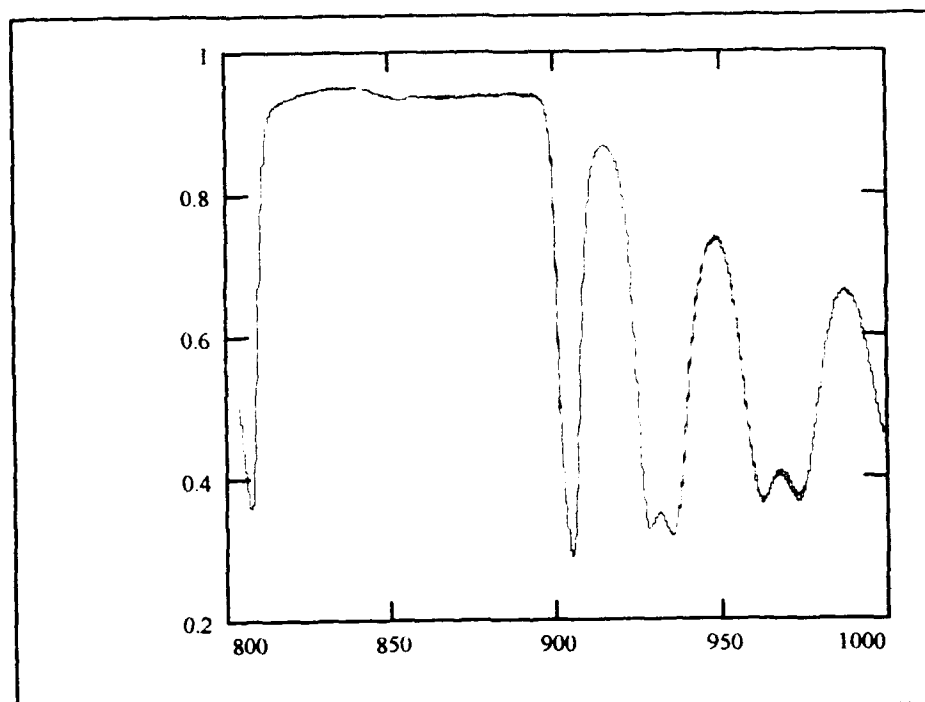   Physical layer thickness: 61.8nm

Figure 4.9. New 3λ reflectivity plot.

4.2.3 InGaAs MQW

This VCSEL was grown at the University of Virginia using MBE and was grown in the <110> crystalline direction. The unique crystalline direction was chosen in an attempt to make output polarization of the VCSEL constant across the wafer. Gain region uses two InGaAs MQW layers with AlGaAs spacers.

Material Parameters:

> Mirror: AlAs and GaAs
> Number of top mirror layers: 16
> Number of bottom mirror layers: 19.5
> Active region: 2 $In_{0.2}Ga_{0.8}As$ MQW layers
> with $Al_{0.45}Ga_{0.55}As$ spacers
> Active region thickness: λ/n
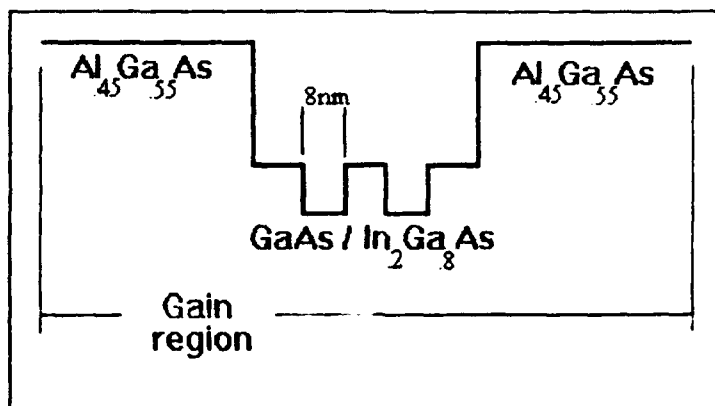> Substrate: GaAs
> Design wavelength: 950nm

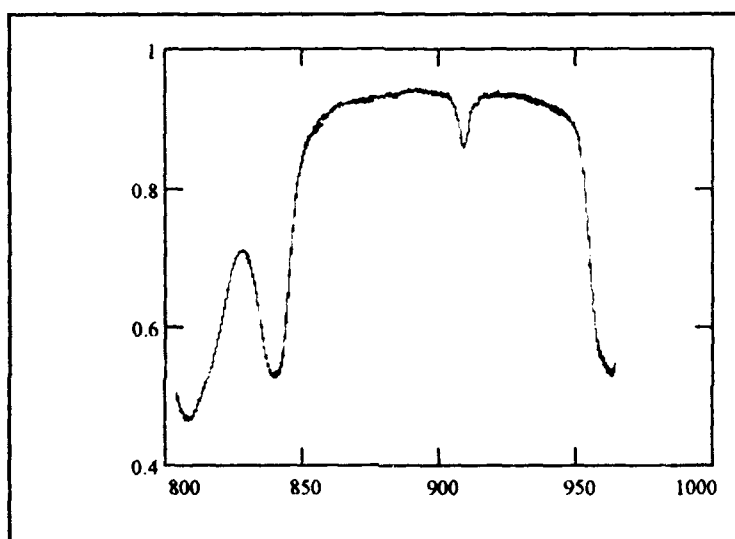Figure 4.10. Architecture of InGaAs gain region.

Figure 4.11. InGaAs reflectivity plot.

4.3 Specifications

<u>Scanning Fabry-Perot Etalon</u>: Burleigh RC-110 with Burleigh RC-44 ramp generator. Mirrors 830-910nm center 870nm

<u>Optical Multichannel Analyzer (OMA)</u>: EG&G Princeton Applied Research Model 1460. OMA Vision-PDA data acquisition/analysis software run on AT&T 386 PC. Grating in OMA is 1200g/mm, 600 blaze.

<u>Acousto-Optic Modulator</u>:
InterAction Corporation Acousto-Optic Modulator model AOM-40N:
     rise time 170ns
     diffraction efficiency 85%
     wavelength range 700 - 1300nm

max drive power 3.5W @ 830nm

extinction ratio >1000:1

InterAction Corporation Light Modulator Signal Processor model ME-40R:

RF output 40MHz carrier ± 0.0025%

Video input modulation frequency 10MHz max

Polarizing Cube:

Big: Melles Griot, 830nm operating frequency, #03PBS065

Small: Newport, 620-1000nm, 05FC16PB.5

Diode Lens: Melles Griot, f_o=14.5mm, spot size 1.85µs, 06GLC003

Oscilloscopes: Tektronix model #7854 and LeCroy model #7200A

Frequency Generator: Wavetek model 801

Temperature Controller: ILX Lightwave model LDC-3722

FND-100: EG&G, BW - 350MHz, Rise time <1ns

Filter: Ealing; 920nm, BW - 13nm, model #35-4647; 830nm, BW - 12.4nm, model #35-4548

Argon-ion Laser: Coherent Innova 400 Sealed Mirror Ion Laser, 30W maximum output power

Ti:Sapphire Laser: Coherent Mira 900 Model 900-P

White Light: Brinkmann, Q-Beam, Halogen Light

Power Meter: Coherent Field Master model FM

Power head: model LM-2 with removable 1000:1 attenuator

VCSEL Translation Base: Line Tool Co, model #102RH; 2µm/division

V. Results and Analysis

In the following section results of the various experiments are provided along with analysis. General observations, including VCSEL response to different pump configurations, and the theory behind negative lensing, are provided first, followed by the characteristics of each VCSEL. Finally, overall observations are provided.

5.1 VCSELs and Pumping

Given the correct pump configuration, the VCSELs would lase nearly anywhere on the VCSEL surface. There were no "special" spots from which all data was generated. In fact, although location data was taken for every spot, each time the system was aligned (which was very often) the location data became meaningless, making it virtually impossible to retake data from a specific spot. Instead, a conscious effort was made to take data from as many different locations on the VCSEL as possible.

5.1.1 **Carrier Populations** As mentioned in Chapter 2, calculation of carrier population is not straight forward, and indeed, we are unable to generate realistic numbers using Equation 2-17. This difficulty is attributed primarily to a lack of a stimulated emission term in the equation. In addition, values need to be estimated for carrier lifetime, material absorption, and illuminated area (increased by an unknown lateral spreading factor). It was hoped that with an estimate for carrier population we could in turn estimate the change in index of refraction due to carrier population by looking at Figure 2.5. It may be possible to calculate the value of Δn from the

equations provided in Bennett [3], but that calculation is beyond the scope of this effort.

5.1.2 Spectral Profiles   In general, each lasing spot has unique lasing characteristics--unique spectrally, temporally, and in intensity. However, some generalizations can be drawn. The four pump configurations listed in Chapter 4 (i.e., CW, gated CW, picosecond, and gated picosecond) produced different output characteristics. The CW pump was the least effective in producing a stable VCSEL output and the picosecond pump, the most.

Figure 5.1 shows a sample of the spectral output from Old 3λ where the vertical axis is amplitude of arbitrary units, the horizontal axis is wavelength in nm. This spectra is typical of a picosecond pump VCSEL. Figure 5.2 shows the spectral output of a spot lasing with three transverse modes. Transverse modes with this separation were fairly common with Old λ3, especially when the iris regulating the pump was fully dilated resulting in a bigger spot on the VCSEL. The reason is that as
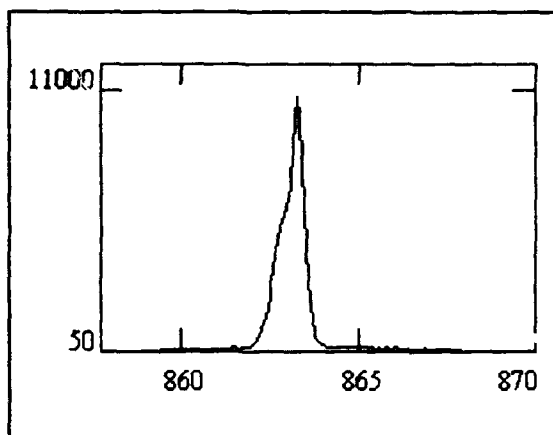

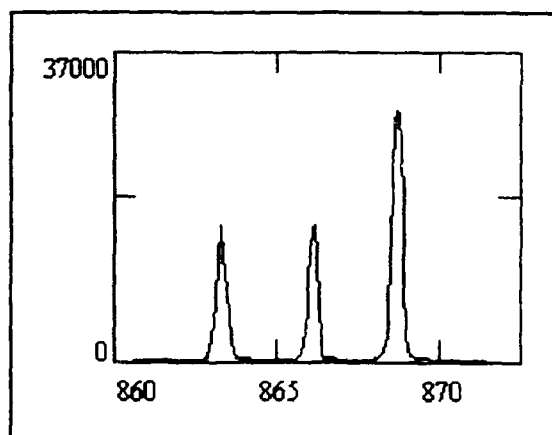Figure 5.1. Spectral output of an Old 3λ spot.

Figure 5.2. Three transverse modes from Old 3λ.

the spot size of the pump is increased, the cavity volume achieving inversion increases
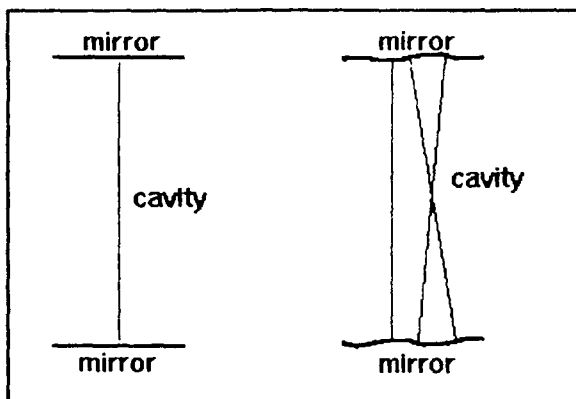

Figure 5.3. Single and multiple transverse mode cavities.

and lasing is possible between more facets of the mirror surfaces (see Figure 5.3). The distance between the facets is slightly different resulting in slightly different output frequencies. Although they may appear so, the modes in Figure 5.2 are not regularly spaced.

Figure 5.4 shows an example of a typical lasing spot for the InGaAs VCSEL using a CW pump. Figure 5.5 shows an atypical lasing spot. The wide spectral width of Figure 5.5 is attributed partially to the spot on the VCSEL (it appears more than one transverse mode is going) and partially to the pump. Because the picosecond pump has a peak power of nearly 8800 times greater than a CW pump (with the same average power), the instantaneous index changes due to carrier injection and the fast heating then cooling of the lasing cavity
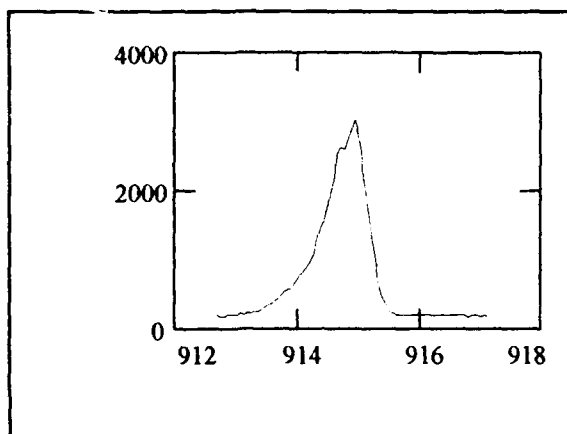

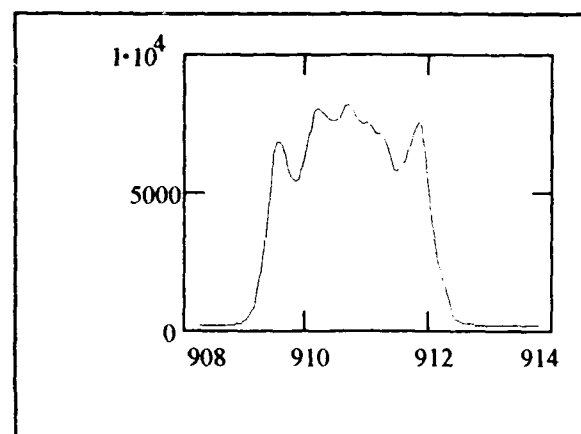Figure 5.4. CW pumped spectral output of an InGaAs lasing spot.

Figure 5.5. Spectra of an InGaAs spot for picosecond pump.

5-3

due to the intense pump produces a transient response of the output wavelength which smears or broadens the output spectrum. This effect can be most easily seen in Figures 5.6 and 5.7 which are photographs of the scanning F-P output. The spectral profile of Figure 5.6 does not have transverse modes lasing as in Figure 5.5, but it is more typical of spots pumped in picosecond mode. In picosecond mode, the peak pump power is not only increased, but because the pulse duration is only 1.5ps, the VCSEL achieves inversion without reaching steady state. Without the conditions of steady state operation as a requirement, nearly all areas of a VCSEL lased when pumped with picosecond. Another effect of the picosecond pump is the lack measurable subthreshold spontaneous emission. The VCSEL output spectra goes from no output to lasing without the wide spectral emission associated with fluorescence and CW pumping (see Figure 5.8). In other words, the OMA shows that the VCSEL begins to lase with a characteristically narrow spectral beam which appears to rise out of the surrounding spectral noise.
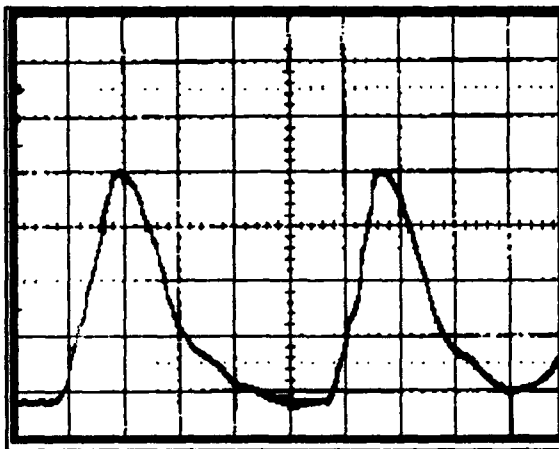

Figure 5.6. Spectral profile of typical VCSEL output pumped in picosecond.

Figure 5.7. Spectral output of CW pumped spot.
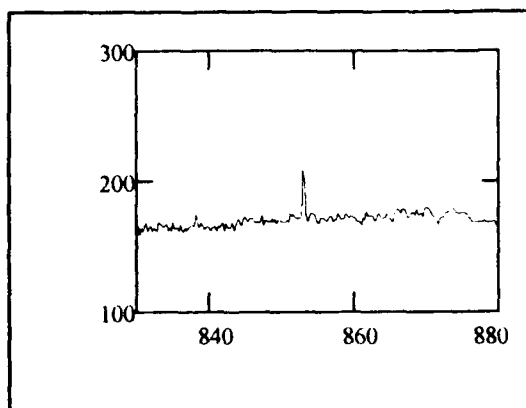
Motion The VCSEL reflectivity plots provided in Chapter 4 reveal that their form does not necessarily conform to the plot generated by the reflectivity model (see Figure 2.2). This is not surprising because VCSEL reflectivity (and lasing wavelength) is strongly dependent on position; i.e., where on the wafer the reflectivity is taken.

Figure 5.8. Narrow spectral output at "threshold" of picosecond pumped VCSEL.

This nonuniformity is due the growth technique of Molecular Beam Epitaxy (MBE) which results in thinner layers of material at the edge of a wafer than in the center; therefore, reflectivity of a VCSEL has a radial spatial dependence. Table 5.1 shows the spectral shift of each VCSEL for a translation in X and Y directions. Additional measurements of New 3λ (chosen because its radial direction could be seen--Figure 5.9) revealed that the ratio of Δλ between radial and tangential directions is 10:1.

Table 5.1. Shift in reflectivity profile as a function of X/Y position

VCSEL	$\Delta\lambda$ (Δd_y = 0.5mm)	$\Delta\lambda$ (Δd_x = 0.5mm)
Old 3λ	1.0nm	1.7nm
New 3λ	1.49nm	3.26nm
InGaAs	1.28nm	2.82nm

An additional factor adding to the challenge of operating the Old 3λ VCSEL was physical movement of the VCSEL on the surface of the mounting plate. With a
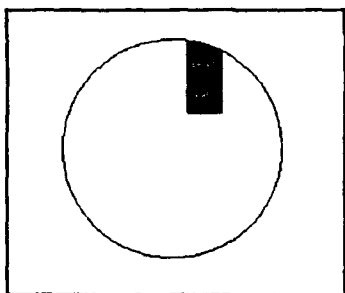
Figure 5.9. New 3λ
orientation on wafer.

change of substrate temperature of ±4°C, the VCSEL would move horizontally up to 5μm and vertically 3μm. This movement is attributed to a pocket of air under the VCSEL.

5.1.4 Polarization and Power Polarization of the VCSEL beam was not necessarily of interest in this effort except that for the wrong polarization, the VCSEL output would not pass through the polarizing cube and into the detection portion of the setup. If the VCSEL output was not detected, it would not be considered a lasing spot. To help measure the polarization, a beam splitter was placed in the input pump path and the reflected energy from the VCSEL was measured (see box labeled "optional" in Figure 4.1). The results are given in percent horizontally polarized (i.e., the percent which passes through the beam splitter). I found the polarization to be primarily oriented such that it passed through the beam splitter. It may be that output polarization of a VCSEL is an inherent function of the VCSEL and is determined completely by the physical orientation of the VCSEL to the detection device; in which case I simply got lucky. Or it may be that VCSEL polarization is primarily a function of the pump polarization; in this case the VCSEL polarization was orthoganal to the input. Or it could be another mechanism (including the very real possibility that the VCSEL output was not even linearly polarized), but to my knowledge no single factor has been identified which determines VCSEL polarization.

Table 5.2. VCSEL polarization in percent horizontal.

VCSEL	Polarization
Old 3λ	93%
New 3λ	83%
InGaAs	99%

Power measurements revealed that the maximum average power out was about

0.3mW and a "good" lasing spot produced about 0.2mW.

5.2 Power Dependent Focus

It was observed that reducing pump power required the vertical position of the

diode (focus) lens be translated lower to maintain *peak* output from a VCSEL. The

phenomenon of power dependent focus is attributed to self-defocusing or negative

lensing effect of the VCSEL material. This phenomenon is traditionally called the

optical Kerr effect, and is given by,

$$\Delta n = \frac{3\eta_o}{n^2\epsilon_o}\chi^{(3)} \qquad (5\text{-}1)$$

where η_o is the impedance of free space, ϵ_o permittivity of free space, and $\chi^{(3)}$ is the

third order nonlinear optical coefficient which is itself related to optical susceptibility

[14:753]. However, we have already stated that $\chi^{(3)}$ effects are not believed to be

great and that the refractive index change due to carrier injection is dominate.

Regardless, the action would the same. Negative lensing occurs when the

semiconductor material decreases its refractive index as a function of the intensity of

the incident beam. Assuming the beam profile is gaussian, then the beam center

passes through the material faster than the outer edges making the wavefront become

spherical or defocused. More specifically, the scenario goes like this: assuming the

optimal excitation of the gain material occurs when the pump energy is focused in the

center of the gain medium, then at higher power the gain region (for the bulk GaAs

VCSELs) has defocused the beam resulting in the focusing lens having to be

positioned further from the VCSEL than geometric optics would require (the VCSEL

is pumped well below the bandedge of the mirror material). As power is decreased,

defocusing is reduced and the focus point moves higher in the VCSEL, decreasing the

coupled power and lowering the output amplitude at a faster rate than anticipated (i.e.,

output amplitude is not linearly related to input power). In addition, the data in the

remainder of this chapter will show that there is no discernable relation between output

amplitude and wavelength shift; therefore, it follows that although negative lensing has

a notable effect on output amplitude, it has none on wavelength shift.

Unfortunately, there are two major inconsistancies with the above argument.

First, although the physical movement of the focus suggests negative lensing, the

magnitude of the movement (on the order of $50\mu m$) would require the index of

refraction to have changed by a factor 38. So either the action within the VCSEL is

more complicated and/or something else is occurring. Second, this power dependent

focus e...ct was experienced in all three VCSELs, but carrier population nonlinearity

was dominate in only one. The two bulk GaAs VCSELs were dominated by

temperature nonlinearities which caused the output wavelength to redshift. So the

question becomes how can the gain material exhibit negative lensing (i.e., a decrease in refractive index) when the overall effect of the VCSEL output is an *increase* in the refractive index. This is clearly a topic for further research.

5.3 VCSEL Nonlinear Responses

The following subsections present the results of the experiments conducted on the three VCSELs. Each section provides some general information including threshold levels and pump and lasing wavelengths. Table 5.3 provides bandedge values for the materials used in the VCSELs. The lines and curves used to fit the data are generated using linear regression and stepwise regression techniques respectively. The equation of each fit-line and values for refractive index changes for all subsequent figures are provided in Appendix A. Error is given as root-mean-squared.

Table 5.3. Bandedge values for materials used in this effort.

Material	Bandgap (eV)	Bandgap (nm)
GaAs	1.424	871.3
AlAs	2.168	572.3
$Al_{0.127}Ga_{0.873}As$	1.5824	784.1
$Al_{0.45}Ga_{0.55}As$	1.9852	625.0

5.3.1 **Old 3λ** Old 3λ was pumped between 820nm and 827nm which is about 0.08eV above the bandgap of GaAs and lased between 856 and 869nm (just *above* the bandgap). Threshold was observed as low as 8.1mW with gated picosecond pump.

5.3.1.1 **Wavelength Dependence**   Figure 5.10 shows data taken from

the same spot on the VCSEL pumped CW then picosecond. As average power

increases, the percent converted into heat remains the same, i.e., the VCSEL (once

lasing) does not become more efficient. As a result, the cavity temperature increases

and we see a linear relationship between wavelength and average power as predicted.

However, the CW trace starts 2nm higher in wavelength than the picosecond data with

the same average power. This is explained as follows. The picosecond pump puts out

1.5ps long pulses, but each pulse is separated by only 13ns and because the material

response to temperature is relatively slow, the cavity temperature is averaged resulting

in a temperature which is the same as the CW pump with the same *average* power.

The off-set is instead attributed to carrier population. The near instantaneous injection

of carriers associated with the picosecond pump pulse increases the bandgap resulting
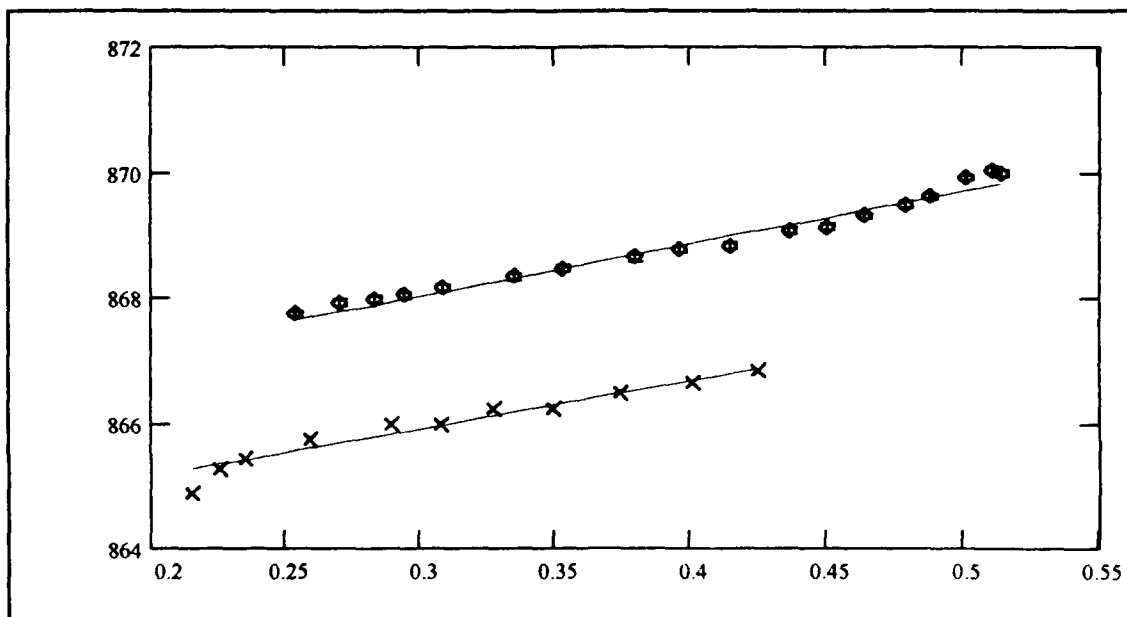

Figure 5.10. Wavelength (nm) vs average input power (W).   ◇ - CW pump;
×- picosecond pump.

in an output which is shifted to shorter wavelengths; even though cavity heating is still

the dominate factor. Also, both fit-lines have nearly the same slope which again

implies that it is the *average* power which determines the cavity temperature and hence

the shift in wavelength as average power increases.

Figure 5.11 shows wavelength vs peak power for data generated by a gated

CW pump of constant 204ns gate width at different gate repetition rates. × and □ are

for a repetition rate of 500KHz but were taken from different spots (approximately

6µm separation). ◇ was taken from yet a third spot and used a repetition rate of

1MHz. Notice that the fit-lines for × and □ have nearly the same slope but are offset

by about 1.3nm. The offset is attributed to the nonuniformity in the VCSEL

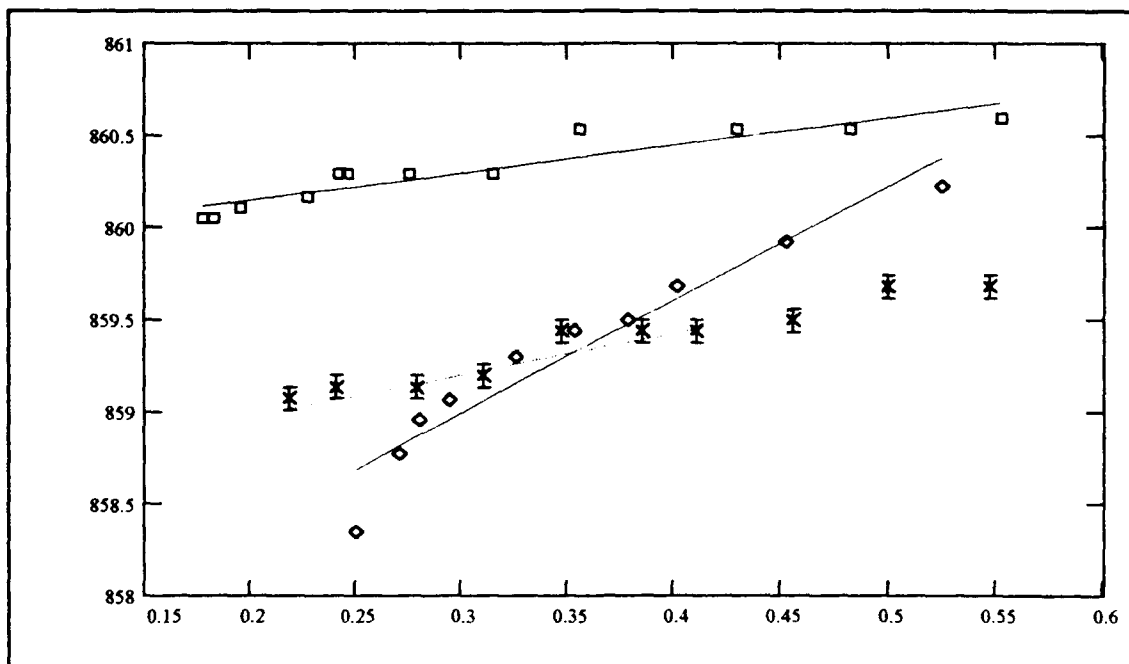architecture (i.e., the spatial separation of the spots result in different starting

Figure 5.11. Wavelength (nm) vs peak power (W). × and □ are for 0.5MHz rep rate
from different spots, and ◇ is for 1MHz rep rate.

frequencies). Likewise ◇ which was taken about 0.6mm away from ✕ and ☐

Obviously the striking feature about Figure 5.11 is that ◇ has a slope 3 to 4 times

greater than the 0.5MHz traces. This difference is anticipated since at a given peak

power, ◇ has twice the average power and greater cavity temperature.

Figure 5.12 shows a linear relationship between wavelength and average input

power for gated picosecond pump. Gate width is constant at 188ns and repetition rate

is varied. Of more interest is the relation between wavelength and time between gates

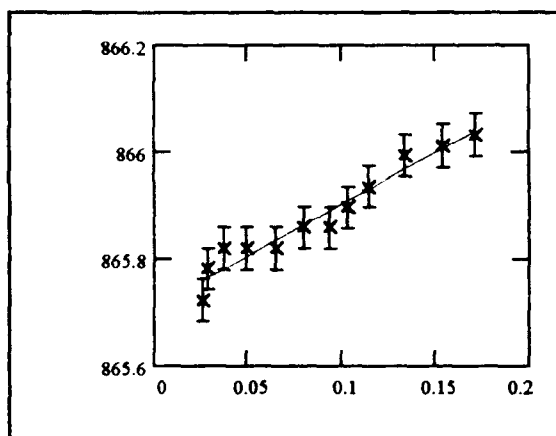(see Figure 5.13). Notice that at intervals of <2µs Δλ is maximum.

Figure 5.12. Wavelength (nm) vs average input power (W) for gated picosecond pump. Repetition rate is varied.

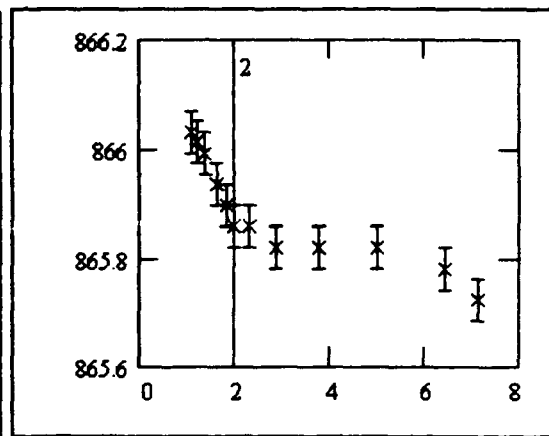Figure 5.13. Wavelength (nm) vs time (µs) between 188ns picosecond gates.

5.3.1.2 Amplitude Dependence The internal power for a saturated

diode laser is given Equation 5-2 where P is power in Watts, η_i is the internal

quantum efficiency, i is the injected current in amperes, i_t is the current required for

threshold, and λ_o is the lasing frequency in µm [14:624]. Figure 5.14 shows

$$P = \eta_i (i - i_t) \frac{1.24}{\lambda_o} \qquad\qquad \text{(5-2)}$$

amplitude output vs average input power for the same data sets as Figure 5.11.

Strangely, each fit-curve has a different shape, none of which are linear as Equation

5-2 predicts. Equation 5-2 says that the steady-state laser internal photon flux is equal

to the injected photons per second in excess of that required for threshold, and that a

linear relationship should exist between average input power and the average output

amplitude. In Figure 5.14, × and □ show a quadratic response and are typical of the

amplitude verses input power data collected for this effort. That is, amplitude is

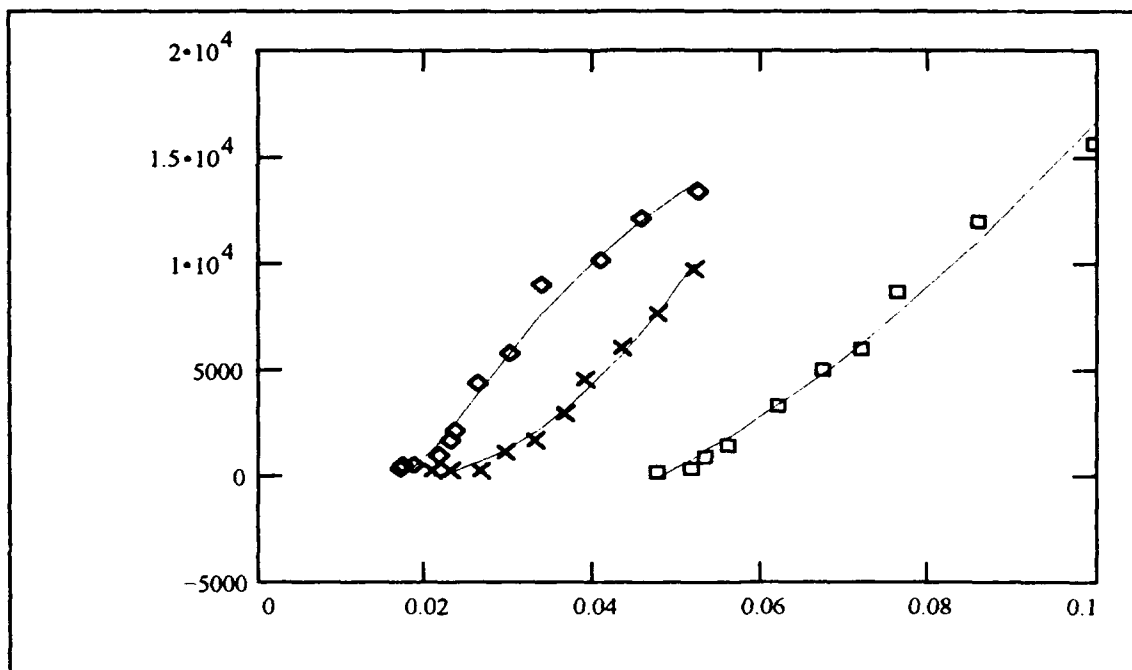related to input power *squared* (at least for × and □; see Appendix A). It is not known

Figure 5.14. Amplitude vs average power. × and □ are for 2μs gated CW pump and
◇ is for a 1μs pump.

what the source is for the additional power dependence. It could be from the negative

lensing effect, but Old 3λ is clearly dominated by temperature nonlinearities. If for

some reason negative lensing were the cause it would explain the shape of ◇. The ◇

data was generated opposite of × and □ in that the focus was optimized for <u>low power</u>

performance and the power subsequently <u>increased</u>. Therefore the data has a $1/power^2$

relation.

An alternative argument is that the ◇ data set is consistent with saturation and

that × and □ are consistent with threshold condition. That is × and □ appear quadratic

because at low output power the laser is making the transition between fluorescing and

lasing. The difficultly with this argument is that the spectral width of the VCSEL

output indicated that it was clearly above threshold at all times.

5.3.1.3 Substrate Temperature Dependence

Increasing the substrate

temperature affects the VCSEL's ability to conduct the heat away from the cavity

volume. The relationship between VCSEL substrate temperature and the output

wavelength is linear as discussed earlier. Figure 5.15 shows two traces corresponding

to two different pump configurations; × is for a CW pump and □ is for a picosecond

pump gated at 2.14μs with a width of 244ns. The ratio between the fit line slopes is

2:1 indicating that the increase in cavity temperature in □ is half that of ×.

5.3.2 New 3λ

New 3λ bulk GaAs VCSEL was pumped at about 803nm

(0.121eV above the bandedge) and lased between 848 and 854n--well above the

bandedge of GaAs and nearly 25nm from the designed lasing wavelength of 875nm.
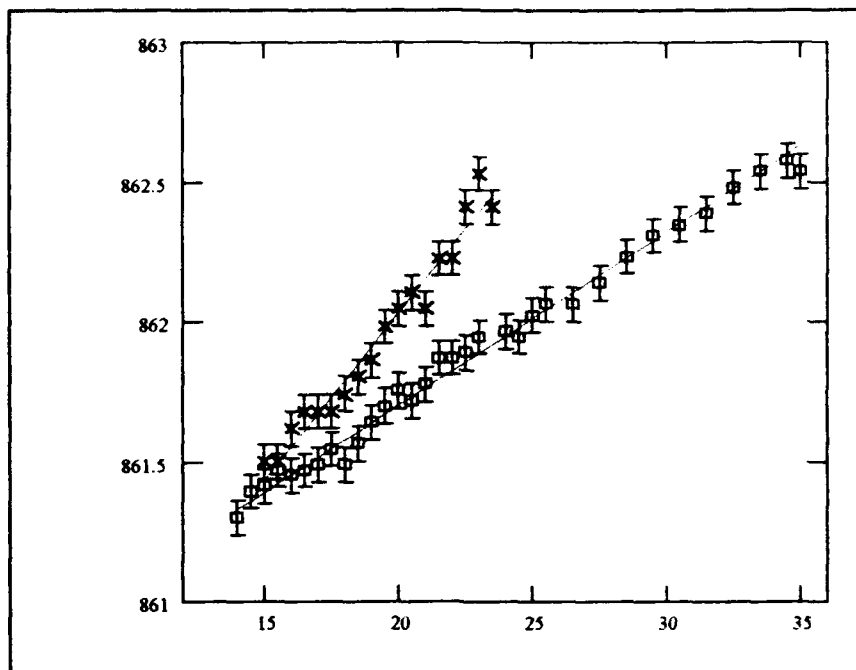
Threshold was as low as 8mW with a gated picosecond pump.

Figure 5.15. Wavelength vs substrate temperature. × is CW and
□ is gated picosecond.

5.3.2.1 Wavelength Dependence   Figure 5.16 shows wavelength versus

average input power for three different pump configurations pumping the same spot.

The first (dashed with ×'s) is a CW pump, the second (dotted with +'s) is a picosecond

pump, and the third (solid with ◇'s) is a gated picosecond pump with a gate width of

190ns and time between gates of 2μs. The purpose of this graph is to show that the

slopes of all three are very similar. However, when graphed with respect to peak

power (Figure 5.17), the difference between the two picosecond pumped data sets

becomes evident. The gated picosecond pump has much less redshifting even though

it is operating at high peak power.

5.3.2.2 Amplitude Dependence   Figure 5.18 shows amplitude versus

peak input power for the same data as Figure 5.17. ◇ has much less amplitude due to

it's low average power (see Figure 5.16).
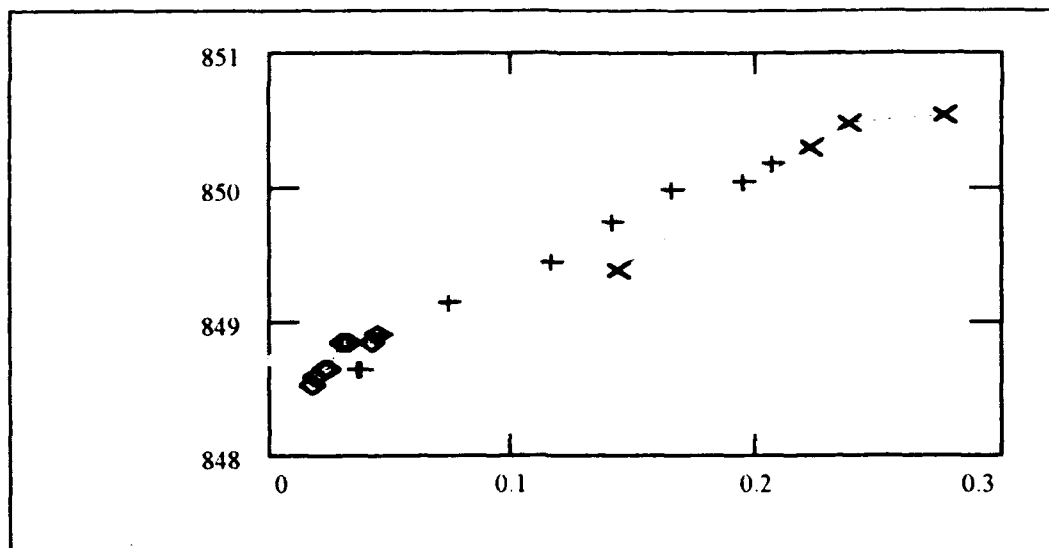
Figure 5.16. Wavelength (nm) vs average input power (W) for CW (dashed), picosecond (dotted), and gated picosecond (solid).

Figure 5.17. Wavelength (nm) vs peak input power (W) for same data as Figure 5.16. + is picosecond, ◇ is gated picosecond.

5.3.2.3 Substrate Temperature Dependence Figure 5.19 shows

wavelength vs substrate temperature (^{o}C) for two different average powers (the upper

trace is 300mW, the lower, 250mW). The offset between the lines was anticipated

because of the difference in the differential cavity/substrate temperatures.
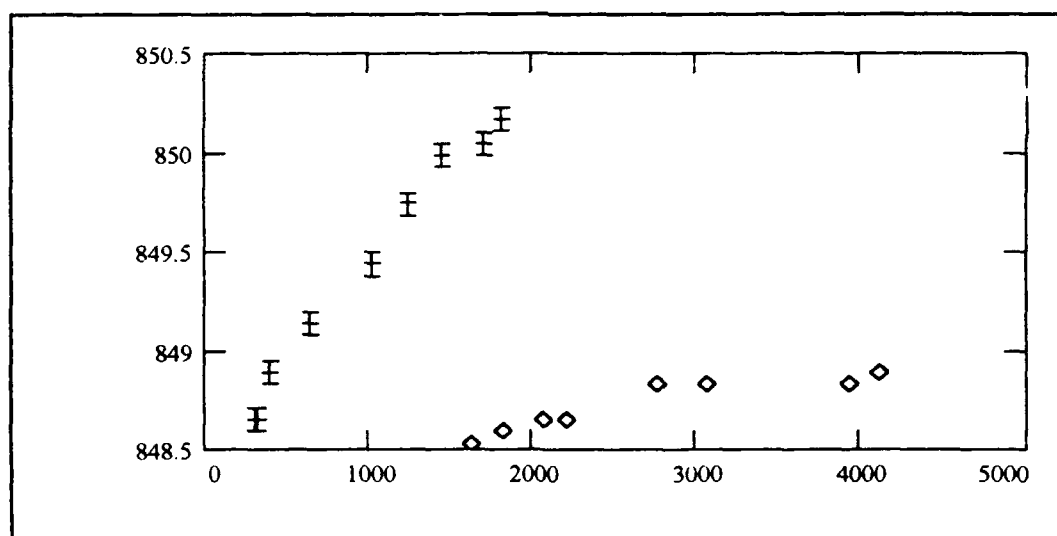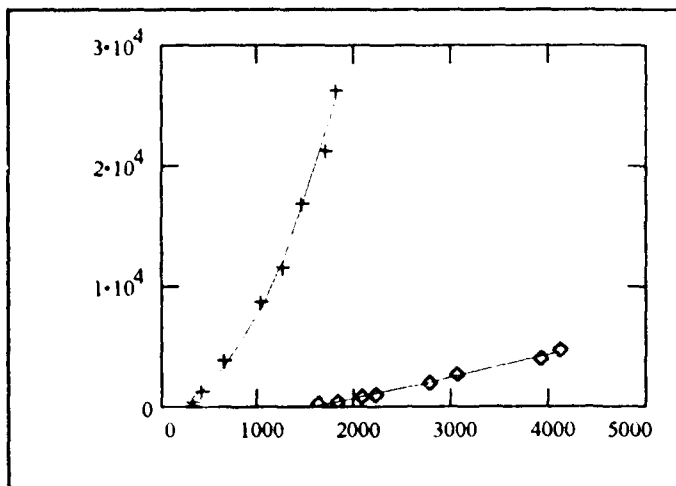
Figure 5.18. Amplitude vs peak input power (W).
+ is picosecond, ◇ is gated picosecond.
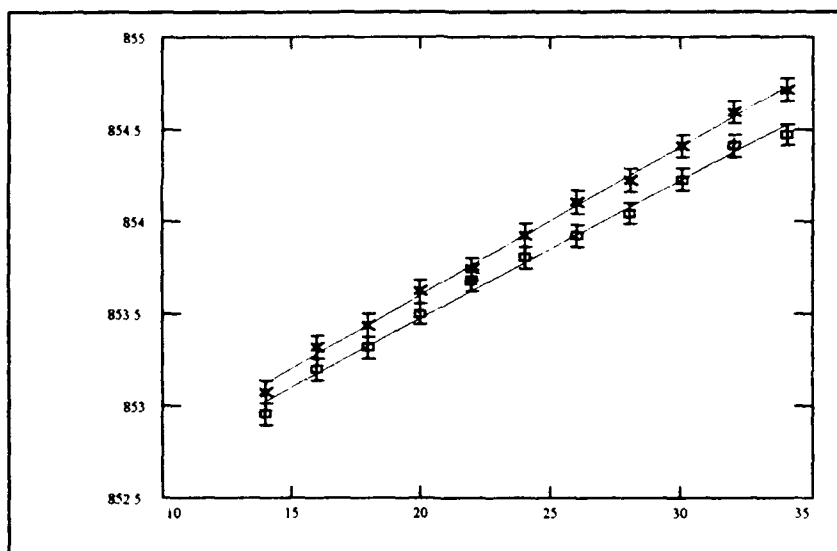
Figure 5.19. Wavelength vs substrate temperature for two different input powers of picosecond pump (×-300mW;□-250mW).

5.3.3 **InGaAs** The <110> InGaAs MQW VCSEL was pumped at wavelengths between 830 and 844nm and lased between 907 to 924nm. Threshold was as low as 0.79mW pumped with gated picosecond versus 259mW in CW. This VCSEL was the

only one to exhibit a well defined F-P dip. By viewing the F-P dip, one could see

that fluorescence and lasing began at wavelengths 4 - 5nm longer than the F-P dip due

to cavity heating.

5.3.3.1 **Wavelength Dependence**   Figure 5.20 shows wavelength vs

time between 194ns gates of picosecond gated pump power into the InGaAs VCSEL.

No redshifting is observed past 5µs and the vertical line marks 2µs which is the repetition rate used for the majority of the experiments in this effort. Notice that at 2µs redshifting due to heating becomes prevalent.
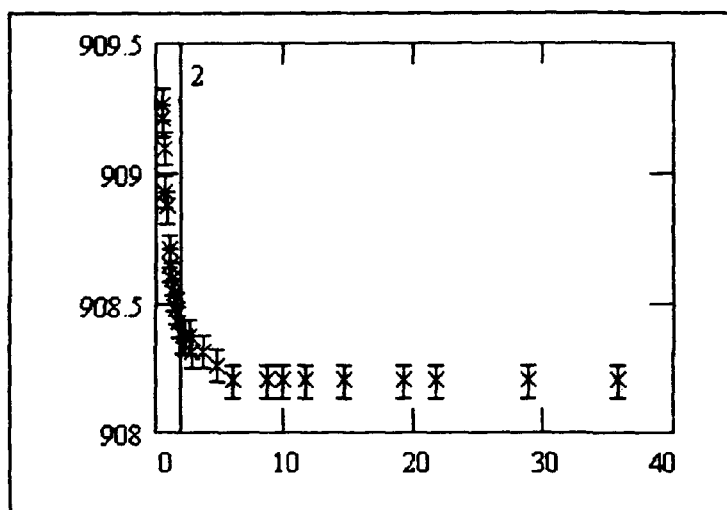
Figure 5.20. Wavelength (nm) vs time (µs) between gates of gated picosecond pump with gate width of 194ns.

Figure 5.21 shows the change in wavelength versus average power for a gated

picosecond pump with three different repetition rates. The data was taken from the

same lasing spot and the uncertainty is the same for all three. Notice two things:

First, the spectra blueshifts with increasing power and gate spacing. This occurs

because although the cavity temperature is essentially the same for a given average

power regardless of the duty cycle (past 2µs), the magnitude of the nonlinearity due to

carrier injection *is* dependant on duty cycle. Figure 5.21 shows that a given trace
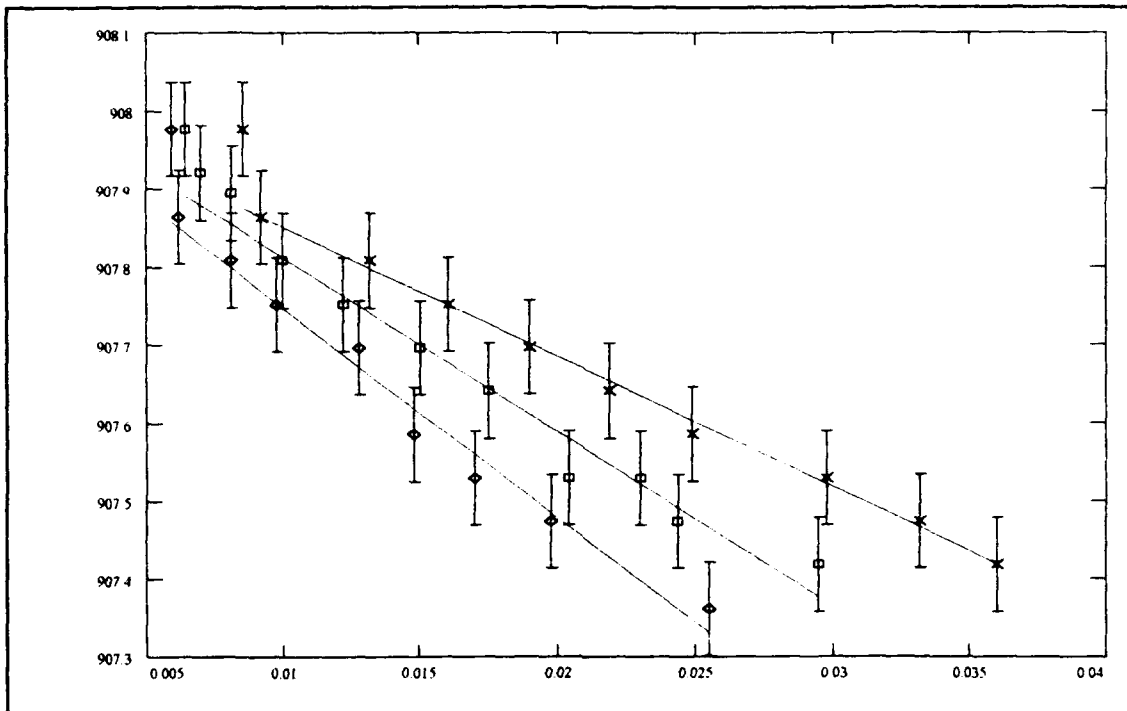
Figure 5.21. Wavelength (nm) vs average power (W). Pump is gated picosecond with a gate width of 190ns and gate spacing of 2.0µs for ×, 2.5µs for □, and 3.0µs for ◇.

exhibits more blueshift at greater peak power (e.g., ◇ at 25mW average power). This point is further illustrated by Figure 5.22 which shows that all three lines fit within the uncertainty of one line indicating that at the same peak power, the blue shift is the same (regardless of the average power).

Second, each trace exhibits a steeper slope at low power (near threshold). This second phenomenon is more difficult to explain. Figure 5.23 shows the trace of × for a clearer view of the characteristic hook found in all three traces and in some other data sets. It is believed that the VCSEL is operating above threshold judging by the spectral profile of the output. However, at low power the internal lasing field is not strong enough to rob the carriers and bring the quasi-Fermi levels closer together--i.e., at greater power the internal field is well established and tends to redshift the spectra.

5-19
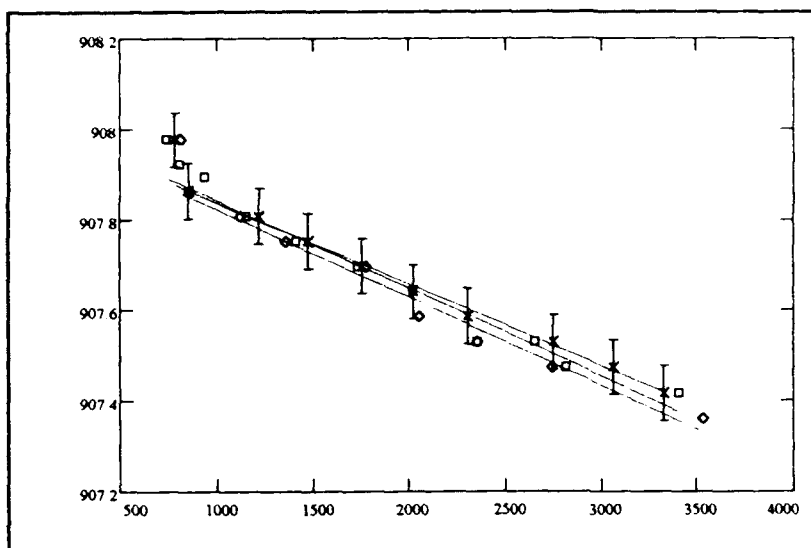
Figure 5.22. Wavelength (nm) vs peak input power (W). Same data as Figure 5.21.

Figure 5.23. Close up of × data from Figure 5.21. Notice the hook at the beginning of the trace.

As the carrier concentration increases, the spectra tends to blueshift more rapidly but is balanced by the redshifting effect of the internal field. As a result, once the internal field is fully established, the spectral response becomes more gradual (the slope decreases).

Figure 5.24 shows wavelength versus average input power for the same spot but pumped with different pump configurations--× is picosecond and □ is picosecond gated with a width of 304ns and a repetition rate of 1.43MHz (0.7μs). The duty cycle used here is well above that used in Figure 5.21 therefore heating is the dominate factor and the output redshifts. Both traces

show redshifting, but □ indicates that heating is reduced to a point that the carrier

induced nonlinearity has reduced the redshift significantly (see Figure 5.25).
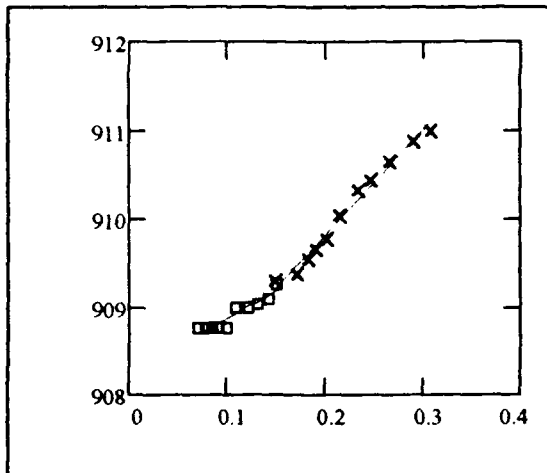
Figure 5.24. Wavelength (nm) verses
average input power (W). □ is gated
picosecond, × is picosecond.
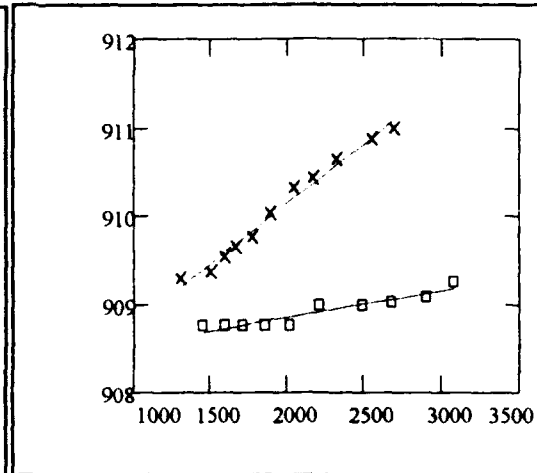
Figure 5.25. Wavelength (nm) verses
peak input power (W) for same data as
Figure 5.24.

Figure 5.26 shows data for a different spot on the InGaAs VCSEL. The solid

line shows wavelength versus average input CW power, where as the dashed line is

for picosecond pump. The slopes are the same but greater than those in Figure 5.24.
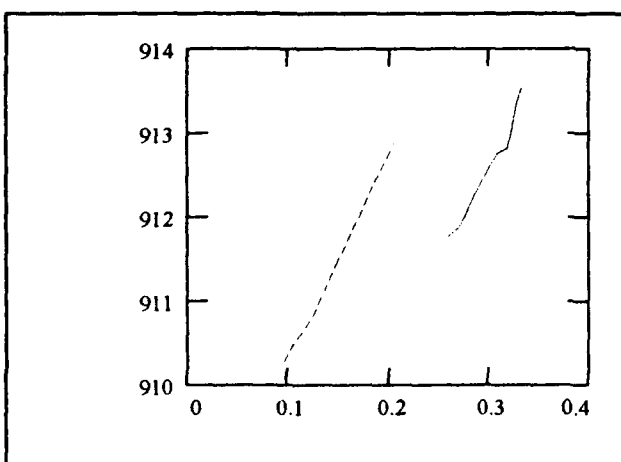
Figure 5.26. Wavelength (nm) verses average
input power to InGaAs. Dashed line is
picosecond pump and solid is CW.

This difference is attributed to this
particular spot. Notice that the
picosecond pump gets the VCSEL
to laser at a much lower average
power. On the other hand, there is
less power available from the
Ti:Sapphire laser in picosecond
mode restricting the pump power to
about 200mw average power.
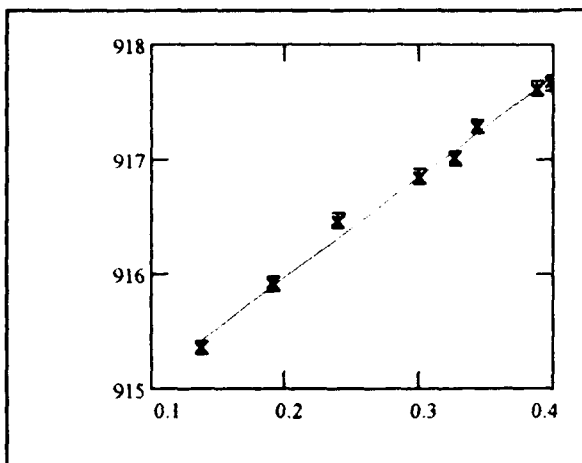
Figure 5.27. Wavelength (nm) of fluorescence vs average input CW power (W).

Figure 5.27 shows the wavelength change of a fluorescing spot versus average input power of the CW pump.

5.3.3.2 Amplitude Dependence

Figure 5.28 shows the amplitude response versus input peak power. As expected, all three data sets begin at the same peak power. And as expected, each trace reaches a different peak amplitude due to the difference in *average* input power. Again, the data is fitted with quadratic fit-lines as shown in Equation 5-4 (equations for all fit lines are fou ⌐ in the appendix). As before, there are at least two interpretations of why there is not a

$$curve \; \diamond \; = \; -6.282*10^6(power)^2$$
$$+ \; 4.762*10^5(power) \; - \; 2169.58$$

(5-4)

linear relationship. First, is that the VCSEL, specifically the QWs, are being saturated as power increases. This argument is reenforced when one looks at the same data plotted wrt average power (Figure 5.29). All three lines lie on top of one another indicating that at a given average power the QWs saturate.

The second possible explanation is that there is a power dependent focus or defocus action within the VCSEL. All previous data has shown a positive quadratic

5-22
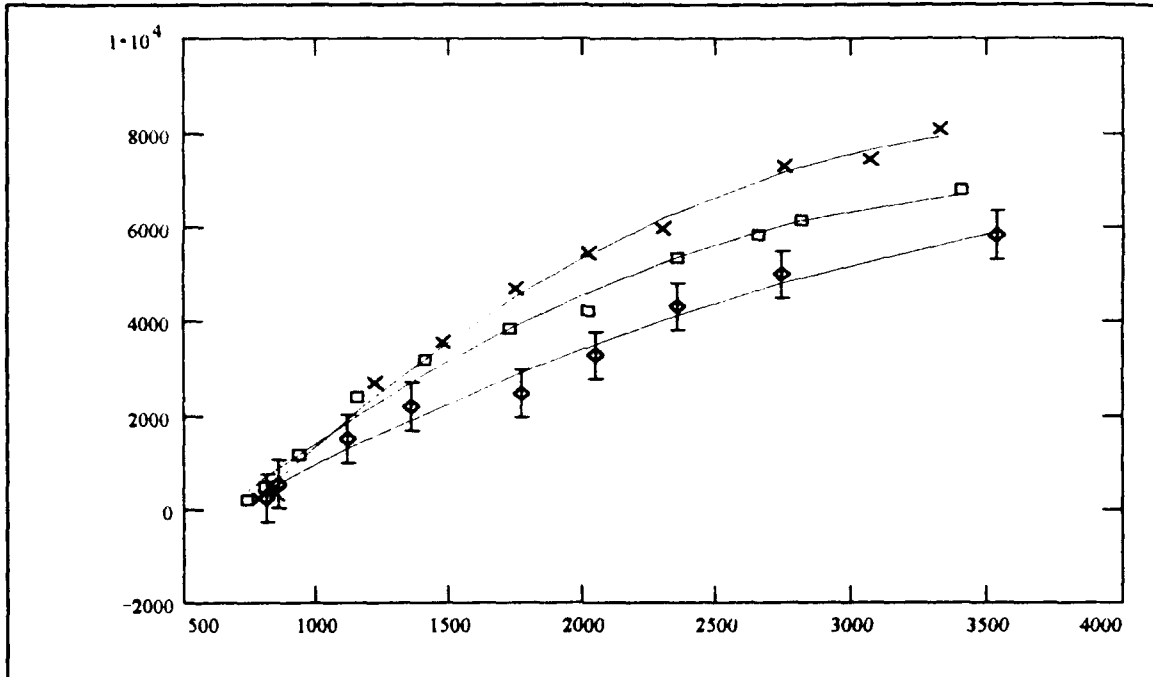
Figure 5.28. Amplitude vs peak input power (W) for same data as
Figure 5.21. Time between gates: × - 2μs, □ - 2.5μs, ◇ - 3μs.

form where as this data shows a negative quadratic form. Obviously, the overall

nonlinear effect in this VCSEL is opposite that of the previous VCSELs. But how the
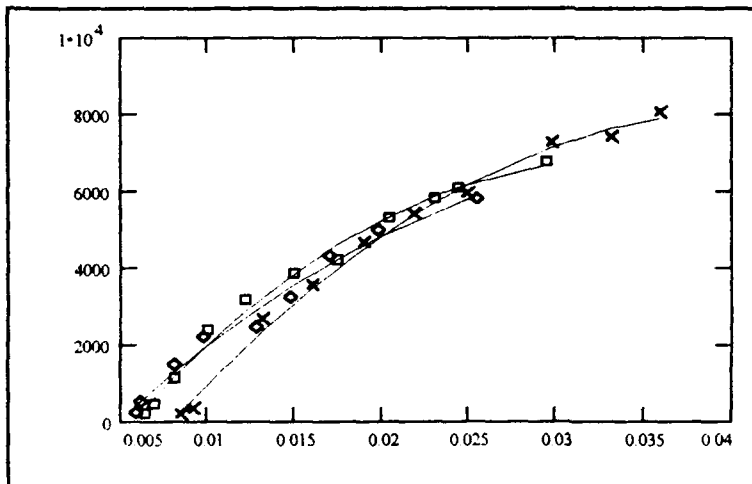
Figure 5.29. Amplitude vs average input power (W) for
same data as Figure 5.21. Time between gates: × - 2μs,
□ - 2.5μs, ◇ - 3μs.

difference in overall nonlinearity could affect the output amplitude in not known. However, it could be that the difference in the shape of the curves between the InGaAs and GaAs VCSELs is due to the

difference in architecture. The mirror layers of the InGaAs VCSEL are made of AlAs/GaAs and the gain region has two MQW layers separated by 8nm GaAs layers (see Figure 4.10). The two MQW layers provide two locations of high gain in the cavity instead of the distributed gain material of the bulk VCSELs. Also, because this VCSEL is pumped at 850nm, the GaAs in the mirror absorbs the pump as well (the VCSEL was designed to be pumped at just below the 871nm bandedge of GaAs). As a result, the GaAs changes refractive index, and the $\lambda/4$ design of the DBR is corrupted reducing reflectivity and increasing the mirror losses.

5.3.3.3 **Substrate Temperature Dependence** Figure 5.30 shows the change in wavelength as a function of substrate temperature for the InGaAs VCSEL. The × data is taken for a lasing spot with the pump in picosecond mode. ◇ is taken of fluorescence with a CW pump. The slope of ◇ is twice that of ×.
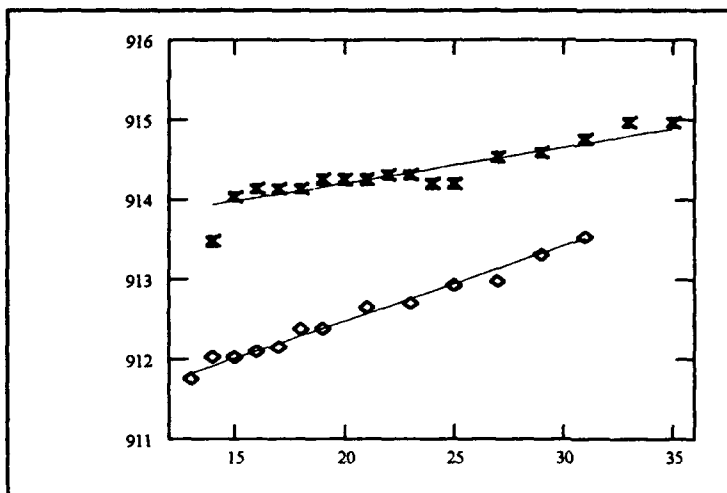
Figure 5.30. Wavelength (nm) vs substrate temperature. × is picosecond lasing and ◇ CW fluorescence.

5.4 **Analysis and Observations**

Although much data has been generated it is difficult to draw sweeping quantitative conclusions about the nonlinear response of the VCSELs. This difficultly

is due to the interplay of the nonlinear mechanisms and the dependence of the VCSEL response on lasing location. However, some general observations are possible.

The maximum change in refractive index was found to be about $+9*10^{-3}$ (see Appendix A). In Jacquet [8], values of Δn are provided for *carrier induced* refractive index changes for electrically pumped bulk lasers. These values range from $-17.5*10^{-3}$ to $-70*10^{-3}$ [8:621]. The best $-\Delta n$ we could get was $1.3*10^{-3}$ using the InGaAs MQW laser. This compares to $-90*10^{-3}$ in Jacquet using separate confinement MQW lasers [8:621]. It is not known why the values for Δn in Jacquet are so high--especially considering that the lasers are electrically pumped (is not apparent whether the electrical pump was pulsed). It is also curious considering that we did not experience the distinct advantage optically pumping promised.

Previous research stated that gate separations of $>1\mu s$ and gate widths of $<100ns$ would eliminate the effects of heating on the VCSEL response. And it appears that gate widths of 190ns and separation of $2\mu s$ accomplish the same goal for the optical setup used in this effort. However, the $1\mu s/100ns$ rule was established for electrically pumped VCSELs which have to overcome joule heating. The duty cycle between electrical and optical pumping are nearly the same meaning that there does not appear to be a significant advantage to optically pump VCSELs. Why is unknown.

Using the value for dn/dT found in Table 2.1, it is calculated that for every 1nm redshift for a bulk GaAs VCSEL, the cavity temperature changes $30^{\circ}C$, assuming contributions to wavelength shift by all other mechanisms are insignificant.

5-25

New 3λ was designed with more mirror layers than Old 3λ with the goal of achieving lower threshold levels. But lowest threshold levels are 8.0 verses 8.1mW respectively which indicate there is very little advantage to the extra mirror layers. In addition, both bulk GaAs VCSELs lased below the 875nm design wavelength and well above the bandedge of GaAs which surely reduces the efficiency of the VCSEL (e.g., the carriers saturate the absorption). The InGaAs MQW VCSEL however, was designed with less than half the mirror layers of the bulk VCSELs but lases at a lower threshold (despite the mirrors absorbing the pump). This greater efficiency is attributed to the QW layers. The QW layers also have a profound effect on nonlinear response. The only nonlinear mechanism which tends to blueshift the spectra is carrier injection and because the InGaAs VCSEL was the only one to blueshift (at any repetition rate) then the additional mechanism of phase filling must be significant.

There appeared to be a nonlinear relationship between input power and output amplitude. This is attributed to negative lensing or it could be due to the characteristic curves associated with the gain saturation and absorption saturation. This may well be a topic for further research.

One of the original goals of this research is to quantify the nonlinear effect due to internal lasing field and determine whether it can be utilized in the design of optical switches or Q-switched VCSELs. Although no numbers for the internal field effects have been generated, it appears that the magnitude of lasing field (a redshifting mechanism) is directly dependent on carrier population (a blueshifting mechanism) and the two mechanisms cancel each other. The blueshift achieved with the InGaAs

VCSEL is attributed to the picosecond pump. The response of the lasing field (based

on the 100ns carrier lifetime) can not respond to the picosecond gate of carriers

resulting in an average carrier level in excess of that found in CW pumped systems.

Also, it does not appear $\chi^{(3)}$ has any noticeable effect. Therefore, it is unlikely that

field effects will be useful in design of new VCSELs. If any nonlinear effect *could* be

shown to produce the effect for Q-switching, the tolerance of any design would

probably exceed the capability of current fabrication technology.

VI. Conclusion

This thesis has presented a detailed account of the theory behind the nonlinear characteristics of VCSEL semiconductor materials and of the VCSEL as a whole. Further, it has generated data which in large part corroborates the theory. The results from this effort could be used in further work characterizing optically pumped VCSELs.

6.1 Review of Nonlinear Mechanisms in VCSELs

There are three nonlinear mechanisms occurring within a VCSEL: cavity heating, carrier injection, and field effects. Heating affects the crystalline lattice spacing which changes the bandgap. Changes in the bandgap change the absorption characteristics which, in turn, effects the net gain. Absorption also affects the index of refraction through Kramers-Kronig relations and as a result changes the lasing wavelength. The approximate change in the index of refraction of GaAs with temperature is $1.36 \times 10^{-4} /°C$. Cavity heat is dissipated into the surrounding material according the coefficient of thermal conductivity and the differential temperature between the cavity region and the substrate material. As a result, there is a linear relationship between the substrate temperature and output wavelength.

Heating effects are generally the dominate nonlinearity in VCSELs. However, these effects can be minimized if the pump beam is pulsed. Pulse widths of about 200ns (FWHM of picosecond pulses) and pulse separation times of $>2\mu s$ were required before the heating effects could be reduced significantly.

6-1

When the effects of heating were reduced to the point they were no longer dominant, nonlinear effects due to carrier population were evident. This is known because carrier population is the only nonlinear mechanism which blueshifts the VCSEL output spectra. In a broad sense, blueshifting results from the quasi-Fermi levels separating as the carrier population increases. More specifically carrier population is responsible for several nonlinear actions occurring within the semiconductor material. These phenomena are known as bandfilling, bandgap shrinkage, and free-carrier absorption. Bandfilling of the lower conduction bands result in bleaching of the absorption in the vicinity of the bandgap. Bandgap shrinkage occurs whe.i the coulomb forces of the electrons in the conduction band act to reduce the bandgap. Free-carrier absorption, also known as the plasma effect, is the result of a photon exciting an electron within a band. Blueshift of the gain profile is also a result of the quasi-Fermi levels separating.

It was shown repeatedly that peak power strongly influenced the nonlinear effect due to carrier injection. A VCSEL produced an output at shorter wavelengths when pumped with a pulsed beam with a short pulse width and higher peak power than the same spot did for lower peak power (provided that average power was the same for both). This dependence can not be attributed to temperature differences as temperature effects can not react on the microsecond level. Cavity temperature instead is the result of average power.

The final nonlinear effect is due to internal field effects. Because VCSELs operate very near the band edge of the gain material, the primary field effect is due to

the field robbing the gain material of its inversion and thus reducing the separation of the quasi-Fermi levels. As the quasi-Fermi levels move closer together, the result is a redshift of the output wavelength. It is concluded that, because the field, and therefore it's effects, are a result of carrier population, the nonlinear field effects are balanced by nonlinear carrier injection effects. As a result, it is not believed the field can produce the effect required for Q-switching.

6.2 VCSEL Response

As stated above the VCSELs with ga ` regions of bulk GaAs did not blueshift regardless of the repetition rate. The MQW InGaAs VCSEL did blueshift. This is attributed to the additional carrier related nonlinearity found in QWs called *phase filling* and to the higher net gain inherent in QW (i.e., the heating was reduced because the VCSEL is more efficient).

Amplitude was expected to be linearly related to input power. It was discovered that there exists a power dependent focus phenomenon which may be due to negative lensing.

It was known that MBE fabrication techniques produced VCSEL wafers which were thinner at the edge of the wafer than in the center. This was confirmed by measuring the shift of a reflected broadspectrum source as the VCSEL was translated. The magnitude of the wafer nonuniformity was significant.

6.3 Further Research

As stated previously, additional research could be conducted concerning the

negative lensing effect. Developing a model for what is occurring within the VCSEL would be a considerable undertaking. However, this research would only be of use for optically pumped devices

It is not believed that the data contained within this thesis was analyzed as thoroughly as perhaps it could. With this thesis as a basis, further research could focus on one VCSEL and attempt to model the nonlinearities affecting it, as opposed to surveying the characteristics of several VCSELs.

Appendix A. Calculated Data

Table A.1. Equations for all fit-curves not linear.

Figure	Symbol	Equation (P = average power)
Figure 5.14 (Old 3λ)	×	$7.79*10^6*P^2 - 2.45*10^5P + 1686.55$
	◇	$8.56*P^{-2} - 1009.71*P^{-1} + 30032.1$
	□	$2.158*10^6*P^2 - 4918.72$
Figure 5.18 (New 3λ)	×	$5.955*105*P^2 + 16.47$
	◇	$8.90*10^5*P^2 + 1.07*10^5*P - 1983.3$
Figure 5.28 (InGaAs) .	×	$-7.34*10^6*P^2 + 6.04*10^5*P - 4313.65$
	□	$-8.89*10^6*P^2 + 5.93*10^5*P - 3053.47$
	◇	$-6.28*10^6*P^2 + 4.76*10^5*P - 2169.58$
Figure 5.29 (InGaAs)	×	$-7.34*10^6*P^2 + 6.04*10^5*P - 4313.65$
	□	$-8.89*10^6*P^2 + 5.93*10^5*P - 3053.47$
	◇	$-6.28*10^6*P^2 + 4.76*10^5*P - 2169.58$

Table A.2a. Slope intercept values of linear fit-lines for all figures with fit-lines. Also Δn values and Δn per W or °C for all Δλ figures.

Figure	Symbol	Slope	Y intcpt	Δn	Δn per W or °C
Figure 5.10 (Old 3λ)	◇	8.4	865.5	0.009	0.036/W
	×	7.6	863.63	0.008	0.038/W
Figure 5.11 (Old 3λ)	×	23.72	858.52	0.0025	0.081/W
	□	15.63	859.85	0.0023	0.064/W
	◇	32.28	857.15	0.0079	0.15/W
Figure 5.12 (Old 3λ)	×	1.92	865.71	0.009	0.0089/W
Figure 5.15 (Old 3λ)	×	0.12	859.63	0.004	$4.5*10^{-4}/°C$
	□	0.062	860.46	0.005	$2.5*10^{-4}/°C$
Figure 5.16 (New 3λ)	×	--	--	0.005	0.037/W
	+	--	--	0.0064	0.038/W
	◇	--	--	0.0015	0.057/W
Figure 5.17 (New 3λ)	+	--	--	0.0064	0.038/W
	◇	--	--	0.0015	0.057/W
Figure 5.19 (New 3λ)	×	0.081	851.99	0.007	$3.5*10^{-4}/°C$
	□	0.075	851.98	0.0064	$3.2*10^{-4}/°C$
Figure 5.20 (InGaAs)	×	--	--	0.002	0.0059/W
Figure 5.21 (InGaAs)	×	16.64	908.02	-0.0012	-0.044/W
	□	22.37	908.04	-0.0012	-0.053/W
	◇	26.97	908.02	-0.0013	-0.068/W
Figure 5.24 (InGaAs)	×	11.88	907.44	0.004	0.023/W
	□	6.12	908.25	0.001	0.013/W
Figure 5.25 (InGaAs)	×	11.88	907.44	0.004	0.023/W
	□	6.12	908.25	0.001	0.013/W

Table A.2b. Slope intercept values of linear fit-lines for all figures with fit-lines. Also Δn values and Δn per W or °C for all $\Delta \lambda$ figures.

Figure	Symbol	Slope	Y intcpt	Δn	Δn per W or °C
Figure 5.26 (InGaAs)	dash	--	--	0.004	0.051/W
	solid	--	--	0.006	0.051/W
Figure 5.27 (InGaAs)	×	8.8	914.20	0.005	0.019/W
Figure 5.30 (InGaAs)	×	0.045	913.30	0.003	$1.5*10^{-4}$/°C
	◇	0.094	910.60	0.004	$2.1*10^{-4}$/°C

Bibliography

1. Adachi, Sadao, "GaAs, AlAs, and $Al_xGa_{1-x}As$; Material Parameters for Use in Research and Device Applications," *J. Appl. Phys. 58 (3)*, R1-R29, (1 August 1985).

2. Bagnell, Richard J. *Design and Characterization of Optically Pumped Vertical Cavity Surface Emitting Lasers*. MS thesis, AFIT/GE/ENP/92D-01. School of Engineering and Physics, Air Force Institute of Technology (AU), Wright-Patterson AFB OH, December 1992 (AD-A258 815).

3. Bennett, Brian R., Richard A. Soref, and Jesus A. Del Alamo. "Carrier-Induced Change in Refractive Index of InP, GaAs, and InGaAsP," *IEEE J. Quantum Electron. QE-26*: 113-121, (January 1990).

4. Dutta, Niloy K., Robert L.Hartman, and W. T. Tsang. "Gain and Carrier Lifetime Measurements in AlGaAs Multiquantum Well Lasers," *IEEE J.Quantum Electron. QE-19*: 1613-1616, (January 1983).

5. Gourley, P. L., S. K. Lyo, T. M. Brennan, and B. E. Hammons. "Lasing Threshold in Quantum Well Surface-Emitting Lasers: Many-Body Effects and Temperature Dependence," *Appl. Phys. Lett. 55 (26)*: 2698-2700, (25 December 1989).

6. Halliday, David, Robert Resnick. *Fundamentals of Physics, 2nd ed., Extended Version*. New York: John Wiley & Sons, Inc., 1981.

7. Hasnain, Ghulam, et. al., "Performance of Gain-Guided Surface Emitting Lasers with Semiconductor Distributed Bragg Reflectors," *IEEE J. Quantum Electron. QE-27* (6): 1377-1385, (June 1991).

8. Jacquet, J, P. Brosson, et. al. "Carrier-Induced Differential Refractive Index in GaInAsP Separate Confinement Multiquantum Well Lasers," *IEEE Photonics Technology Lett. 2 (9)* : 620-622 (September 1990).

9. Jensen, B. and A. Torabi. "Temperature and Intensity Dependence of the Refractive Index of a Compound Semiconductor," *J. Opt. Soc. Am. 2 (9)*: 1395-1401 (September 1985).

10. Jin, R., K. Okada, B. Khitrova, H. M. Gibbs, M. Pereira, S. V. Koch, and N. Peyghambariam. "Optical Nonlinearities in Strained-Layer InGaAs/GaAs Multiple Quantum Wells," *Appl. Phys. Lett. 61 (15)*: 1745-1747 (12 October 1992).

11. Lee, Y. H., H. M. Gibbs, S. V. Koch, and N. Peyghambariam. "Physics and Nonlinear Device Applications of Bulk and Multiple Quantum Well GaAs," *Quantum Well and Superlattice Physics 792*: 128-133 (1987).

12. Pankove, Jacques I. *Optical Processes in Semiconductors*. New York: Dover Publications, Inc., 1975.

13. Peyghambariam, N. Class handout of unknown text, Modern Semiconductor Optics, University of Arizona.

14. Saleh, Bahaa E. A. and Malvin C. Teich. *Fundamentals of Photonics*. New York: Wiley & Sons, Inc., 1991.

15. Yariv, Amnon, Pochi Yeh. *Optical Waves in Crystals*. New York: Wiley & Sons, Inc., 1984.

16. Swaminathan, V, A. T. Macrander. *Materials Aspects of GaAs and InP Based Structures*. Englewood Cliffs, NJ: Prentice-Hall, Inc., 1991.

Vita

Captain Scott L. Brown was born on 20 April, 1962 in Cincinnati, Ohio. He graduated from William Henry Harrison High School, Harrison, Ohio in 1980. In September of that year he entered the Electro-Mechanical engineering program at Cincinnati Technical College. He graduated with honors in 1982 and received an Associate of Applied Science degree. In December 1983 Captain Brown enlisted in the Air Force and was trained as an Aircraft Control & Warning (AC&W) radar technician at Keesler AFB, MS. He was subsequently assigned to the 1839th Engineering and Installation Group at Keesler AFB. While there he was accepted into the Airmans Education and Commissioning Program (AECP) and in June 1985 entered the Electrical Engineering program at Louisiana Tech University in Ruston, LA. In 1988 he graduated *Magna Cum Laude* with a B.S.E.E. and subsequently entered Officer Training School where he was commissioned in June 1988 with an AFSC of 4935 (communications engineer). Captain Brown's first assignment was to Falcon AFB, CO where he held a position as an Air Force Satellite Control Network Communications Engineer. In May of 1992, Captain Brown entered AFIT.

Captain Brown is a member of the Eta Kappa Nu engineering Society.

Permanent address: 8136 Strimple Rd
                    Cleves, OH 45002

REPORT DOCUMENTATION PAGE		*Form Approved* OMB No. 0704-0188

Public reporting burden for this collection of information is estimated to average 1 hour per response, including the time for reviewing instructions, searching existing data sources, gathering and maintaining the data needed, and completing and reviewing the collection of information. Send comments regarding this burden estimate or any other aspect of this collection of information, including suggestions for reducing this burden, to Washington Headquarters Services, Directorate for Information Operations and Reports, 1215 Jefferson Davis Highway, Suite 1204, Arlington, VA 22202-4302, and to the Office of Management and Budget, Paperwork Reduction Project (0704-0188), Washington, DC 20503.

1. AGENCY USE ONLY (Leave blank)	2. REPORT DATE December 93	3. REPORT TYPE AND DATES COVERED Master's Thesis
4. TITLE AND SUBTITLE CHARACTERIZATION OF NONLINEAR EFFECTS IN OPTICALLY PUMPED VERTICAL CAVITY SURFACE EMITTING LASERS		**5. FUNDING NUMBERS**
6. AUTHOR(S) Scott L. Brown, Captain, USAF		
7. PERFORMING ORGANIZATION NAME(S) AND ADDRESS(ES) Air Force Institute of Technology WPAFB OH 45433-6583		**8. PERFORMING ORGANIZATION REPORT NUMBER** AFIT/GEO/ENP/93D-01
9. SPONSORING/MONITORING AGENCY NAME(S) AND ADDRESS(ES) Capt Christopher Keefer (RL/OCPA) Rome Laboratories Griffiss AFB, NY 13441		**10. SPONSORING/MONITORING AGENCY REPORT NUMBER**
11. SUPPLEMENTARY NOTES		
12a. DISTRIBUTION/AVAILABILITY STATEMENT Approved for public release; distribution unlimited		**12b. DISTRIBUTION CODE**

13. ABSTRACT *(Maximum 200 words)*

The nonlinear characteristics of optically pumped Vertical Cavity Surface Emitting Lasers (VCSELs) are identified, isolated, and quantified. Three different VCSELs are evaluated including two with gain regions of bulk GaAs operating at 875nm and one multi-quantum well (MQW) InGaAs VCSEL operating at 950nm. The nonlinearities evaluated include those due to cavity temperature, carrier injection, and internal lasing field. The VCSELs are pumped by a picosecond/femtosecond Ti:Sapphire laser which is configured to operate in CW, gated CW (minimum gate width was 200ns), picosecond, and gated picosecond modes. A linear relationship is shown between wavelength and substrate temperature, cavity temperature, and injected carriers. It is shown that heating is the dominate nonlinearity in the bulk gain region VCSELs for the pump duty cycles which could be achieved. The MQW VCSEL was dominated by nonlinearities due to carrier population at duty cycles of 10% or less causing the VCSEL to blueshift. A nonlinear relationship is shown between input power and output power and is attributed to the optical Kerr effects in the mirror layers and gain region.

14. SUBJECT TERMS Semiconductor lasers, nonlinear response, VCSEL, optical pumping, GaAs			**15. NUMBER OF PAGES** 89
			16. PRICE CODE
17. SECURITY CLASSIFICATION OF REPORT Unclassified	**18. SECURITY CLASSIFICATION OF THIS PAGE** Unclassified	**19. SECURITY CLASSIFICATION OF ABSTRACT** Unclassified	**20. LIMITATION OF ABSTRACT** UL

NSN 7540-01-280-5500